Tip-enhanced Raman Spectroscopy: a preliminary study
and
Force Spectroscopy of Collagen Matrices

by

©Katie Brown

A thesis submitted to the Department of Chemistry in partial fulfillment of the requirements for the degree of

M.Sc.

Memorial University Newfoundland

Memorial University of Newfoundland

February 2022

St. John's Newfoundland

Abstract

This thesis contains preliminary work on tip-enhanced Raman spectroscopy (TERS). TERS is a spectroscopy technique that uses AFM and Surface-enhanced Raman spectroscopy (SERS) to achieve nanoscale images accompanied by chemical maps. TERS can be used to identify compounds that cannot be detected with conventional Raman, such as those masked by fluorescence. Raman of retinal tissues, specifically, Raman of vitamin A (retinol) within the tissues, has been of interest within the Merschrod group, and steps have been taken within this thesis to work toward this goal. Computational Raman spectra of vitamin A and its derivatives have been completed to assist in identifying these compounds within the tissues. Biological tissues have many different components that can be detected, and vitamin A has many different products as it is degraded by light and air. These spectra can help distinguish peaks of these compounds, making analysis easier.

The second part of the thesis covers force spectroscopy of collagen. Collagen is one of the main components of cell culture matrices. Previous studies indicate that changing the collagen overlay within the matrices can affect cell behaviour. The mechanical properties of these overlays may cause a change in the behaviour. It is also known that biological tissues have a change in mechanical properties when probed at different length scales. Using atomic force microscopy (AFM), I investigate the effect of tip radius on Young's modulus (stiffness) of three different collagen matrices:

fibrils, PBS collagen and HANKS collagen. The indentation studies indicate that increasing the radius of the indenter decreases the measured Young's modulus of the sample. This suggests that the fibrils in the matrices are stiffer while the network of the matrices is softer and allows more stretching. These results tell us about the multi-scale properties of tissues.

Acknowledgements

First, I'd like to thank Dr. Erika Merschrod for letting me continue to work in her group to finish my Masters degree. I appreciate all of her advice, encouragement and support over the past few years. It has been a pleasure being one of her students.

I'd also like to thank all the Merschrod group members, past and present for all their help with experiments, analysis and presentations.

Finally I'd like to thank the Natural Science and Engineering Research Council of Canada (NSERC), Canada Foundation of Innovation (CFI), the School of Graduate studies (SGS), the Faculty of Science, and the Department of Chemistry for their funding, and the Atlantic Computational Excellence Network (ACEnet) for the computational resources.

Table of Contents

List of Tables

List of Figures

List of Abbreviations and Symbols

E	energy
AFM	Atomic Force Microscopy
TERS	Tip Enhanced Raman Spectroscopy
SERS	Surface-Enhanced Raman Spectroscopy
SPM	Scanning Probe Microscopy
E	Young's Modulus
DFT	Density Functional Theory
RPE	Retinal Pigment Epithelium
EF	Raman enhancement factor
NA	Numerical aperture
JKR	Johnson-Kendall-Roberts
ECM	Extracellular matrix
SCFS	Single-cell force spectroscopy

Part I:

Tip-Enhanced Raman Spectroscopy: a preliminary study

Chapter 1

Tip-Enhanced Raman spectroscopy of mouse retinas: Background

This thesis covers two projects: tip-enhanced Raman spectroscopy of eye tissue (ended due to the pandemic), and force spectroscopy of collagen matrices.

1.1 The Eye

The eye is responsible for vision. It converts light into electrical signals, which are decoded by the brain to produce the images we see. This light conversion involves multiple layers in the retina, each with unique materials properties that can be studied.

The eye is protected by the skull and connected to the body by orbital muscles [1]. The eye consists of three main layers; the front outer layer is the cornea, and the back outer layer is the sclera; this layer provides additional protection to the eye from infections and injuries [2]. The middle layer is the uveal tract which contains the choroid.

The choroid provides nutrients to the retina and contains the iris. The iris controls

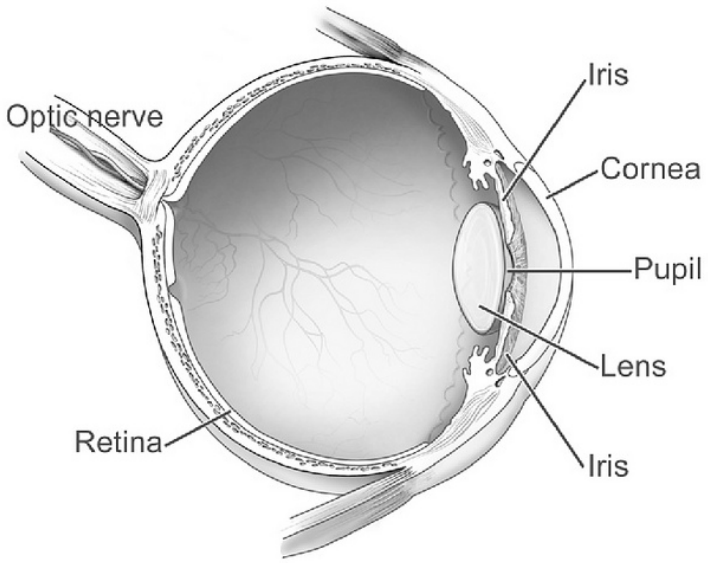

Figure 1.1: Diagram of the human eye. National Institutes of Health, public domain.

the amount of light entering the retina by expanding and contracting the pupil, which affects the image's quality. Before the last layer, there is the lens; this component focuses the light onto the retina, affecting the quality of the image seen.

This brings us to the last layer, the retina. The retinal layer contains the optic nerve, photoreceptors and retinal pigment epithelium for turning light into images. In addition to these layers and parts, there is the vitreous and aqueous humor. This liquid helps control the pressure within the eye and provides additional nutrients. [3] A labelled image of the eye can be seen in Figure 1.1.

1.2 Retina

The retina is the layer responsible for absorbing the light that enters the eye and transmitting it to the brain via the optic nerve. The retina is composed of 10 sheets;

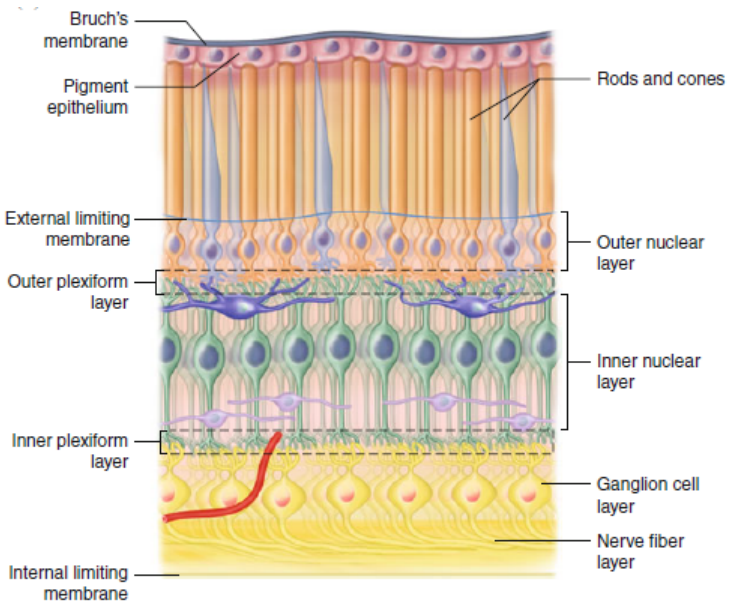

Figure 1.2: Layers of the human retina [5].

the outer layer is the retinal pigment epithelium (RPE) [2, 4]. The next layer is the photoreceptor layer; these are the rods and cones that give us colour and night vision. Next is the outer limiting membrane, which contains the inner parts of the photoreceptors then the outer nuclear layer. Next is the outer plexiform layer, then the inner nuclear layer and adjacent is the inner plexiform layer. Next is the ganglion cell layer, then the inner limiting membrane, which separates the vitreous humor and the retina. See Figure 1.2 for image of retinal layers.

The entire retina is composed of a few areas, the macula, the fovea and the optic disk, seef Figure 1.3 for image of retina. The macula is a small area that is particularly sensitive to light. It is also known as the yellow spot. This functions to protect the eye by absorbing the harmful blue light entering. The fovea is enclosed in this area, where the nuclear layers are thinner, and the ganglion layers are thicker. There are no rods in this area, only cones making it the area of highest visual acuity. This is caused by the 1:1 ratio of cones to ganglion cells. The cones are most abundant in this area and decrease as you move to your peripheral vision [1, 2] There are three

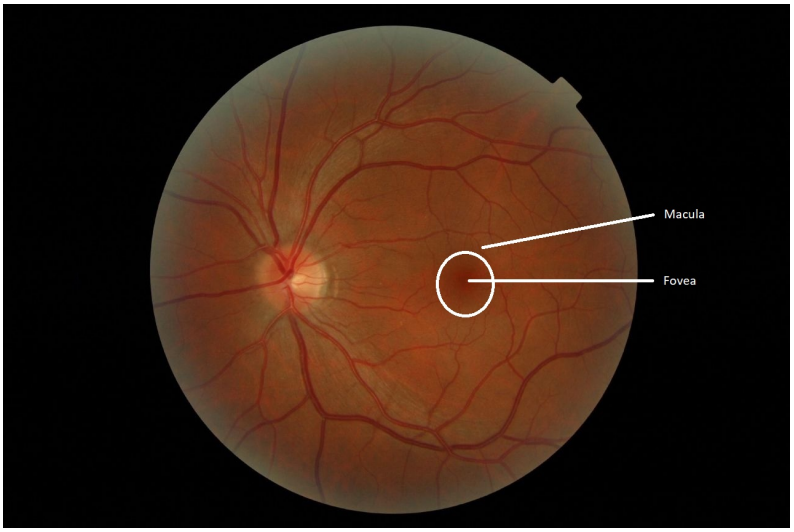

Figure 1.3: Image of the retina. Fovea is located at the right side within the circle with the macula just outside. Richard Masoner, CC BY-SA 2.0. Edited to include labels of the macula and fovea

types of cones; each response to various wavelengths of light. When light is directed on them, the L-type cone has a peak at 560nm; the S type absorbs at 420nm and the M type peak at 530nm. Together these types of cones give us trichromatic vision; they respond to different wavelengths of light. If one or more is absent, it will lead to colourblindness. [1]

1.3 Vitamin A

Vitamin A, also known as retinol (Fig 1.5), is a fat-soluble vitamin found in our bodies, known to aid in vision and the immune system. There are two primary sources of dietary vitamin A, animal tissues and plants. These sources have varying derivatives that the body can convert into a bioavailable source. Animal tissues have preformed vitamin A (retinyl esters, Figure 1.4). This is absorbed by the body and transported to the liver, where it is stored as retinyl esters. This storage can then be transported to the plasma as an alcohol and circulated to the tissues. Plant material contains

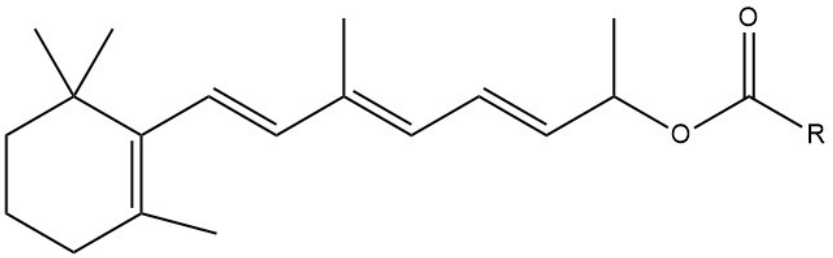

Figure 1.4: Retinyl ester

carotenoids like β-carotene, known as pro-vitamin A. Vitamin A can be formed by an oxygenase found in the intestines.

1.3.1 Derivatives

There are two derivatives of retinol, retinal and retinoic acid. Retinal is primarily involved in the visual cycle, and retinoic acid is needed in the development of many other systems in the body.

1.3.1.1 Retinal and the Visual Cycle

Retinal, as both its cis and trans isomers, is critical for the functioning of the visual cycle. Its production and consumption is located within the RPE. It is thought that the processes that occur in the Muller cells are supplying the cone with 11-cis-retinal (Figure 1.6), but the visual cycle in cones is not widely known. [6]

However, the visual cycle for rods has been extensively studied for years. It starts with 11-cis-retinal covalently bonding to rhodopsin. Light can then be detected; light absorption causes conversions and the release of all-trans-retinal. Membrane-bound dehydrogenases reduce the all-trans-retinal to all-trans-retinol in the photoreceptor cells. Once in the RPE, it is bound and acylated, creating an all-trans-retinyl-ester. This ester is then hydrolyzed and isomerized to form 11-cis-retinol, then taken up by cellular retinaldehyde binding protein and oxidized to 11-cis-retinal. 11-cis-retinal

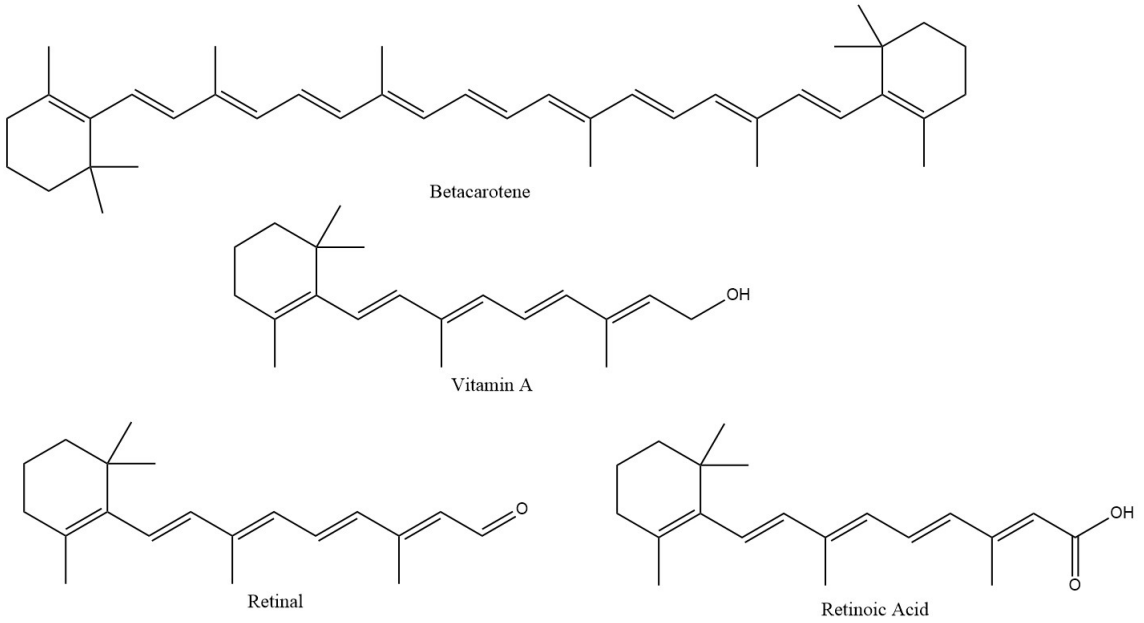

Figure 1.5: Each compound has a very similar structure but each has a different functional group. Vitamin A is an alcohol, retinal is an aldehyde and retinoic acid is a carboxylic acid. β-carotene is the structure that the body converts into each of these compounds.

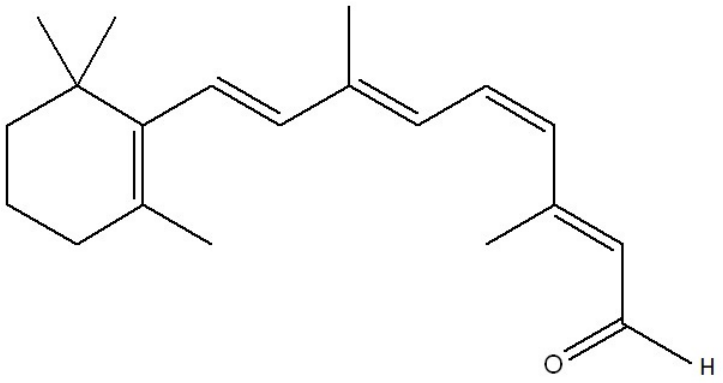

Figure 1.6: 11-cis-retinal is one of many cis isomers of retinal (See Figure 1.5).

is taken up and transported to the RPE and back into the photoreceptor cells. It can then be used again for a different rhodopsin, and the process can be started again. [7,8] If during these processes all-trans-retinal is not fully reduced to all-trans-retinol then, it may result in retinal degenerative diseases such as Stargardt's disease and age-related macular degeneration. [9]

As stated above, 11-cis-retinal is very important to the visual cycle, but it has also been shown that other cis retinoids can be bound to opsins as well. 9-cis-retinal and 9,13-cis retinal were shown to be functional but have a quantum yield of half of that of 11-cis-retinal.

1.3.2 Reactivity

Vitamin A, its derivatives, and related compounds tend to be highly reactive to air, light, heat and acidic compounds. [10] In their crystalline form, retinol, retinal, and retinoic acid are yellow-orange in colour while β-carotene and its derivatives are red-brown.

In a paper by Failloux et al., vitamin A1 was studied using Raman spectroscopy. [11] It found that when retinoid solutions were irradiated with UVA light, both with and without exposure to oxygen, the degradation was the same; however, when aerated, the damage was twice as fast. When exposed to UVB, with and without oxygen, degradation happened three times more slowly without oxygen when compared to the UVA irradiation. Similar to UVA, UVB degraded the retinol at the same rate with oxygen exposure.

Vitamin A produces several photoproducts under certain conditions. Some of these photoproducts include 5,6-epoxyretinol, 13,14-epoxyretinol, 5,8-epoxyretinol, anhydrovitamin A, kitol and all-trans-5,8-peroxyretinol. Wavenumber shifts for these compounds can be seen in Table 1.1.

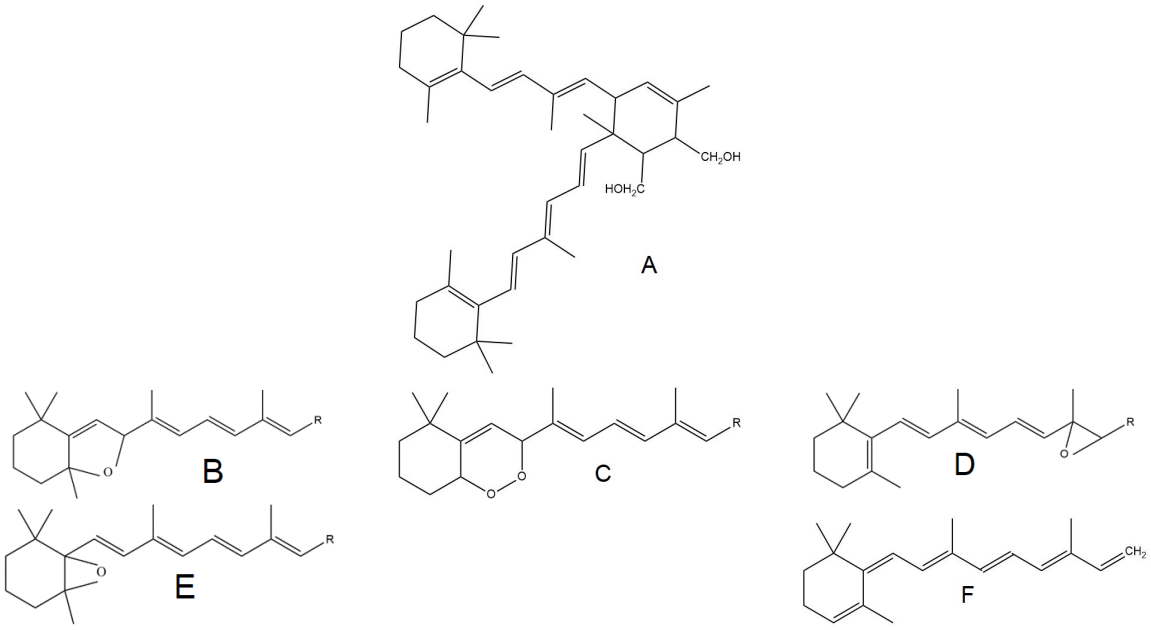

Figure 1.7: Kitol (A), 5,8-epoxyretinol (B), All-trans-5,8-peroxyretinal (C), 13,14-epoxyretinol (D), 5,6-epoxyretinol (E), anhydrovitamin A (F). Each compound is a product of vitamin A after being exposed to light or air.

Anhydrovitamin A is formed with and without oxygen. It can also be formed after the synthesis of retinal. 5,6-epoxyretinol, 13,14-epoxyretinol, 5,8-epoxyretinol are oxidation products, and kitol is believed to be a photodimer of retinol, see Figure 1.7 for chemical structures.

1.3.3 Related Compounds

1.3.3.1 Lutein and Zeaxanthin in the Macula

Lutein and zeaxanthin are the two main xanthophyll carotenoids located in the macula and are responsible for the yellow pigment; see Figure 1.8 for structure. [12] These carotenoids are very similar in structure to pro-vitamin A, but they do not function the same. They cannot be cleaved to form vitamin A due to OH groups on the terminal rings. [13] Lutein is found at a higher concentration in the central region of the macula, and zeaxanthin is concentrated in the fovea. These carotenoids have

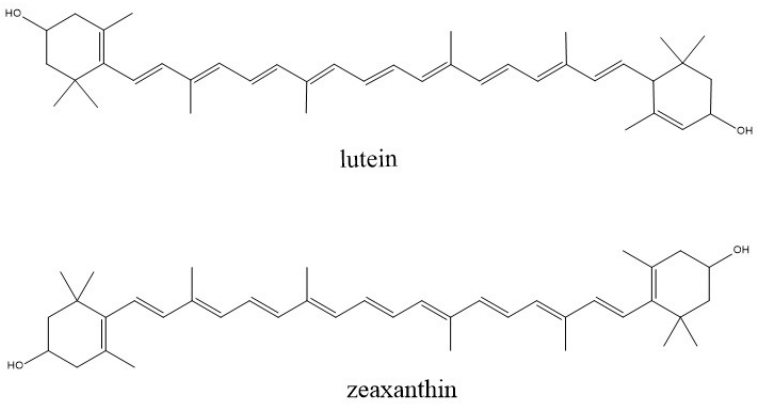

Figure 1.8: Lutein (top) and zeaxanthin (bottom) are compounds located in the macula and fovea of the retina.

several important properties that make them crucial for the retina's health. [12] The first quality that makes these compounds important is their ability to filter blue light. The cornea and the lens of the eye absorb almost all UV-A and UV-B light, but some blue light can pass through to the macula. Lutein and zeaxanthin act as a filter for this blue light; they have an absorption band at 450nm [14] and can mitigate the damage to the retina [15] and slow age-related macular degeneration [13].

Lutein surpasses zeaxanthin in filtering the light due to its orientation in the bilayer of the retina; the hydroxy group is either vertical or horizontal with respect to the bilayer. With the two lutein molecules at right angles to each other, it allows the light to be absorbed from all directions. The zeaxanthin molecules are oriented perpendicular to the layer. Collectively they both filter out a significant amount of blue light and are more effective than beta-carotene, and lycopene [13]

The second defining feature of lutein and zeaxanthin is their antioxidant properties. When short-wavelength light enters the eye, it can generate free radicals and reactive oxygen species and damage the retina. Macular pigments and retinal are particularly good for absorbing and preventing the formation of these free radicals and singlet oxygen species. These pigments are thought to quench the free radicals

in the photoreceptor region because of the presence of retinal and lipofuscin [16–18]. Lipofuscin is undesirable at higher concentrations in the retina because it causes incomplete digestion of oxidatively damaged photoreceptor membranes. It acts as a chromophore and, when hit with light, can generate ROS [19]. Lutein and zeaxanthin can decrease the amount of lipofuscin and suppress damage to the RPE cells. [20]

1.4 Raman Spectroscopy

Raman spectroscopy is a type of vibrational spectroscopy used to identify compounds based on bond vibrations. Raman spectroscopy is widely used across many different disciplines for its ability to analyze compounds of different phases in a non-destructive manner [21, 22].

1.4.1 Raman Scattering

Raman Spectroscopy uses a monochromatic laser to excite the molecules of the compound being analyzed. This causes molecular dipoles to oscillate and scatter photons of different energies. The light emitted can be Rayleigh or Raman scattered light. Rayleigh light is the most abundant light emitted during this process, and it is equivalent to the energy of the laser used. This can also be called elastic scattered light.

In both types of scattering, the photons absorb energy and enter an excited state. A new photon is created and is scattered by a transition from the excited state to a lower vibrational state. The photon exhibits inelastic scattering; the scattering intensity is less than the incident laser intensity. This difference in energy is detected and plotted based on the Raman shift, as seen in equation 1.1. [23]

$$\Delta\nu = \frac{1}{\lambda_0} - \frac{1}{\lambda_1} \tag{1.1}$$

where λ_0 is the wavelength of the incident beam and λ_1 is the wavelength of the scattered photon.

1.4.1.1 Polarizability

For a vibration to be Raman active, it must cause a change in the polarizability of the molecule. This occurs when the molecule is placed in an electromagnetic field; the protons will attract the negatively charged electric field, resulting in the molecule's polarization. This can be stated as

$$\mu = \alpha E \tag{1.2}$$

where μ is the induced dipole moment, E is the strength of the electric field, and α is the polarizability. Polarizability can be defined as the deformation of an electron cloud when an electric field is acting upon it. Molecular vibrations that cause polarizability change are Raman active. [24, 25].

1.4.1.2 Selection Rules

All molecules have various degrees of freedom. These are vibrations of the bonds within the molecule. The vibrations can cause a change in the dipole moment within the molecule which the Raman spectrometer then detects. Two main selection rules indicate how many vibrations a molecule will have. The first, $3n$-6 for non-linear molecules and $3n$-5 for linear molecules, where n is the number of atoms in the compound, and 3 represents the x,y and z-direction. The second part of the selection rules describes the motions a molecule can make, i.e. rocking, bending, wagging, etc. These degrees of freedom are significant when doing Raman spectroscopy because they can affect whether or not the molecule or motion will be Raman active.

1.4.2 Raman Spectroscopy of Vitamin A and Derivatives

Failloux et al.'s study on effects of light, oxygen and concentration on vitamin A shows Raman spectra of retinol solution after decomposition; they found many bands between 1500 and 1700 $cm^{-1}$for vitamin A and its products [11]. They found bands at 1593, 1575 and 1560 $cm^{-1}$for retinol, retinal and anhydrovitamin A, respectively. Another study from Pacia et al. on liver steatosis diagnostics using Raman spectroscopy found bands at 1588 $cm^{-1}(\nu(C{=}C))$, 1202 $cm^{-1}(\nu(C\text{-}C))$, 1155 $cm^{-1}(\nu(C\text{-}C))$ and 1008 cm^{-1}(p(C-CH2)) [26]. A resent study by Mazurek et al. show the peak at 1591 $cm^{-1}$is the C=C stretch of the carbon chain [27]. See Table 1.1 for list of bands and assignments. Band positions from each paper may vary depending on the composition of the sample used.

Table 1.1: Raman shifts for vitamin A and related compounds

Compound	**Wavenumber Shift (cm^{-1})**	**Assignment**
Retinol	1008	p(C-CH2)
Retinol	1155	ν(C-C)
Retinol	1202	ν(C-C)
Anhydrovitamin A	1560	
Retinal	1575	
Retinoic Acid	1582	
Retinol	1588	ν(C=C)
Retinol	1591	C=C
Retinal	1660	
Retinoic Acid	1690	

1.5 Atomic Force Microscopy

Atomic force microscopy (AFM) is a type of Scanning Probe Microscopy (SPM) used to scan and measure surface features with high accuracy and resolution. AFM is a versatile technique, and it can image different types of samples from metals to

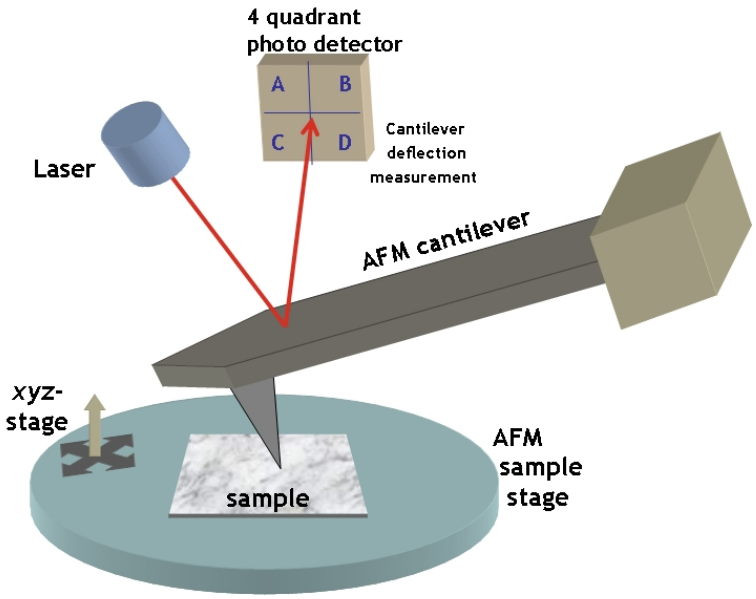

Figure 1.9: AFM set-up for imaging. Taken from the Opensource Handbook of Nanoscience and Nanotechnology

biological materials and image samples in different media such as water and air. Because of its ability to image a variety of samples in ambient conditions, it is used in many different disciplines, including chemistry, biology, medicine, nanoscience, and many more [28].

To achieve atomic resolution, you need many different components [29]. Piezoelectric transducers, often called piezo, the force sensors, and the feedback loop, are three components that are crucial for the AFM to produce high-resolution images. Another critical factor for high-resolution images is the short-range van der Waals forces between the tip and sample when landing the AFM metal tip and the sharpness of the metal tip itself.

To perform a scan, the sample is inserted into the holder located on the AFM stage, and then the tip is placed in the instrument [29]. Once that has been done, the laser is aligned on the end of the cantilever. The laser is deflected onto the photodiode, where it is centred, and then the laser beam is sent to the detector, as seen in figure

1.9. The piezo is responsible for moving the sample stage while performing the scan. A voltage is applied to both ends of the piezo and causes an expansion of the device and movement of the stage. The scan can be completed, and the resolution can be adjusted by choosing the number of points and lines performed in the x and y direction.

As mentioned above, the force transducer is another essential part of the AFM system. It measures the force between the tip and the surface. When the tip is in contact with the surface, the force on the tip is measured, and the voltage output increases; this is where the feedback loop is essential. The feedback loop functions to maintain a constant force between the tip and the sample. To do that, it takes the force signal and sends it to the piezo to set the distance between the tip and the sample in the z direction so the tip can freely scan in the x and y direction. The feedback loop also takes deflection information from the photodiode. This will be further explained in section 1.5.1

1.5.1 Contact Mode

Contact mode was the original mode developed for AFM use [30]. This mode can obtain high-resolution images in a shorter time than other modes. Contact mode operates by keeping the tip in constant contact with the sample [31].

To do this, the tip is brought close to the surface, and initially, there is no net force on the tip or the sample. Then as it approaches, it feels the attractive forces of the van der Waals force and then it will snap-to-contact with the surface. The tip will continue to approach the surface; as this happens, there is a shift from an attractive force to a negative force, which means the tip is now exerting a force on the sample.

The imaging will occur at a chosen set-point within the repulsive regime to avoid damage to the tip or the sample. Hooke's law is used to describe the force on the

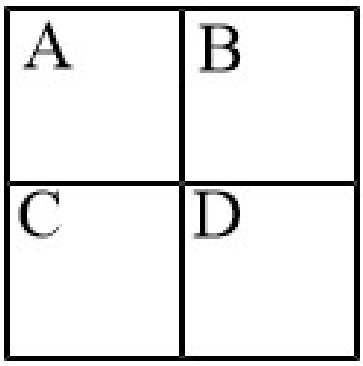

Figure 1.10: Schematic of photodiode.

sample and the laser deflection,

$$F = -kx \tag{1.3}$$

where F is the force, k is the spring constant of the tip, and x is the deflection distance.

The feedback loop mentioned above is important for contact mode because it uses the deflection data to determine the distance the piezo must move to maintain constant deflection/tip-sample force [32]. The deflection results from the forces between the tip and sample, such as the van der Waals forces. These forces cause twisting and bending of the cantilever, which causes the laser path to the photodiode to change. This information is sent to the feedback loop, and then the z piezo is moved.

When scanning a sample, the laser is deflected on the photodiode. The photodiode typically has four segments that can be labelled as A, B, C and D, see Fig 1.10. To determine the vertical deflection, the difference in signal from each segment (a voltage or current) is taken using the following equation 1.4,

$$\text{Deflection} = (A + B) - (C - D) \tag{1.4}$$

Lateral deflection is measured by Eq 1.5

$$\text{Deflection} = (B + D) - (A + C) \tag{1.5}$$

1.5.2 Force Spectroscopy

Force spectroscopy is a technique used to analyze the mechanical properties of various samples. The sample can be indented using an AFM tip, and properties such as elasticity, adhesion, and surface forces can be measured.

The tip is moved towards the sample using the piezo during an experiment, similar to a regular AFM scan. The tip moves towards the sample; as the tip gets closer to the sample, the attraction due to the van der Waals forces increases, eventually exceeding the spring constant, and the tip jumps into contact with the surface. The tip continues until it reaches the force set by the user. Once this point is reached, the tip is retracted back to the initial distance from the surface. The resulting graph is a deflection displacement curve, seen in Figure 1.11. This can be converted to a force-distance curve using Hooke's law, see equation 1.3. Various mechanical properties can be found using the force-distance curve, stiffness, adhesion strength, and it can be used to identify forces between the tip and sample.

Stiffness can be reported by finding the value of the slope of the approach line. Also, adhesion can be found by looking at the difference between the baseline of the retraction line and the bottom of the graph.

In a study by Franz et al., [33], single-cell force spectroscopy studies (SCFS) were done on a variety of cells to investigate cellular mechanics. During an SCFS, a living cell is attached to the tip of the AFM metal tip and approaches a substrate or another cell. A force measurement is completed, and a force curve is made. This type of application allows the force measurement to be obtained at a lower, more sensitive

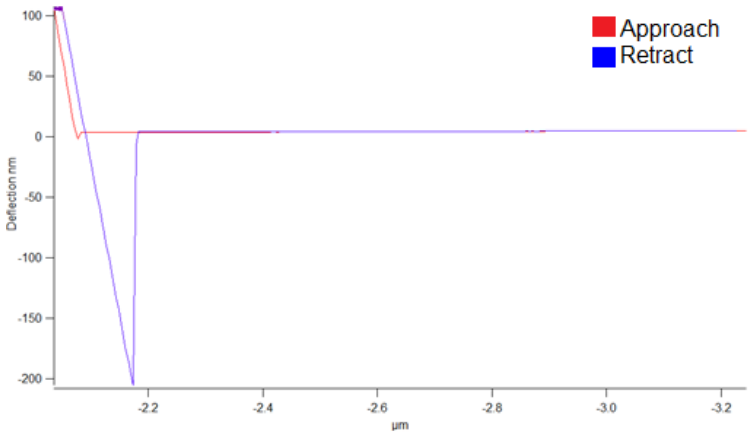

Figure 1.11: Example AFM deflection - displacement curve

force than typical methods. This method can detect forces as small as single receptor-ligand pair unbinding.

Another exciting application for force spectroscopy is in the paper by Fortier et al. [34]. This paper analyzes force indentations of leukemia cells at different indentation lengths and applied forces. They found that increasing the applied force increased the stiffness when probed with a spherical and cone tip. At different indentation lengths, the Young's modulus had a range of values, with the smallest length having the largest Young's modulus and the largest length having the smallest.

When taking a force curve, there is an option to have a dwell time. This is a specified amount of time that the tip sits on the sample's surface at a constant force. How the sample reacts to this sustained force, further indentation or retraction, is called creep deformation/indentation. Creep is the time-dependent elastic behaviour of a sample.

1.6 Tip Enhanced Raman Spectroscopy

Tip-enhanced Raman spectroscopy (TERS) is a spectroscopy technique that uses AFM and Surface-enhanced Raman spectroscopy (SERS) to achieve nanoscale images accompanied by chemical maps. As with Raman spectroscopy and AFM, TERS can be utilized by many disciplines to analyze various samples.

TERS is known for its considerable field enhancement because of the use of a sharp metal AFM tip. Lateral resolution can be as low as 10 nm when the AFM tip size is sufficiently small. Without the near-field optics and the tip enhancement, the resolution would be limited to half the wavelength of light due to the Abbe diffraction limit,

$$\Delta x = \frac{0.61\lambda}{NA} \tag{1.6}$$

where Δx is the diffraction limit, and NA is the numerical aperture. The enhancement in TERS spectroscopy makes it possible to analyze and obtain chemical and structural information with nanoscale samples [35, 36].

1.6.1 Localized Surface Plasmon Resonance and Enhancement Factors

TERS enhancement using a metal AFM tip has the same basic principles as the more commonly known Surface Enhanced Raman Spectroscopy (SERS) effect. [37] The electromagnetic enhancement is caused by the excitation of surface plasmons on spherical/elongated nanoparticles of the AFM metal tip when exposed to light. When surface plasmons are enhanced, the electromagnetic fields surrounding are enhanced if resonance conditions are met. [38]

Another critical effect at play is the electrostatic lightning rod effect. When the incident beam is polarized parallel to the tip apex, a high charge density generates a

high electromagnetic (EM) field at the tip apex. Surface plasmon resonance is generated at the apex if the wavelength of the incident beam resonates with the metal. The energy absorbed results in the surface-enhanced plasmon polaritons. The oscillating polaritons cause the high electromagnetic field seen in TERS. The combination of these effects enhances the spatial resolution found in TERS. [39, 40]

Studies have shown that enhancement decays exponentially with increased tip-sample distance [41]. The evanescent wave formed at the tip apex decays, and the Raman signal decreases [41, 42]. Many factors cause this decay, such as tip and substrate material, tip shape and size, tip-substrate distance, set-up configuration, and polarization of the incoming laser [43].

Finite difference time domain computational methods are used to determine the enhancement factors and decay of gold TERS tips. The enhancement factor of an AFM tip at any position is equal to the fourth power of the electric field. This means the enhancement factor of a gold tip is 1.6×10^5. If a gold substrate is used, the enhancement increases to $1.8\text{x}10^9$. The tip-substrate interaction dramatically increases the TERS signal, and this is in part due to the exponential decay of enhancement with distance [43].

The next factor impacting enhancement decay is tip size. When all other variables such as type of polarized light, incidence angle, tip-substrate distance and wavelength of the laser is the same, but the tip size is changed, the enhancement is relatively constant. There is a slight increase in enhancement with a tip radius between 15 to 50 nm.

There are many different configurations for TERS set-ups, which will be explained further next. These configurations have varying incidence angles, which has a role in enhancement. FDTD simulations show the optimal angle of incidence to be between 40-60 ° for a 632.8 nm laser with p-polarized light. This is due to the interference

of the reflected field being in phase with the incident field; when the incident angle is 90 degrees, the incident beam the reflected field is out of phase and lower the intensity of the light. When changed to s-polarized light, the enhancement factor is negligible because the incidence beam is never in phase to cause excitation of the surface plasmons [40, 43].

Although you do not need a metallic substrate, it has been shown to increase surface enhancement. Gold substrates have the highest enhancements because of the large EM coupling with the tip [43].

The polarization of light affects the evanescent field at the apex of the tip. A signal enhancement occurs when the light is polarized along the tip axis. Large enhancements can cause new selection rules making Raman inactive vibrational mode Raman active [44].

To calculate the enhancement of the Raman signal using the near and far-field electric field intensities,

$$I = \frac{{E_{NF}}^4}{E_{FF}} \tag{1.7}$$

where I is the Raman intensity, E_{NF} is the near-field electric field and E_{FF} is the far-field electric field. Raman enhancement factor (EF) can be calculated using the following formula,

$$EF = \frac{I_{\text{Tip-in}} I_{\text{Tip-out}} - 1}{\frac{A_{FF}}{A_{NF}}} \tag{1.8}$$

where $I_{\text{Tip-in}}$ and $I_{\text{Tip-out}}$ are the Raman intensities with the tip in and out of contact with the sample. A_{FF} is the laser spot size, and A_{NF} is the area of the TERS tip, πr^2 where r is the tip radius [45].

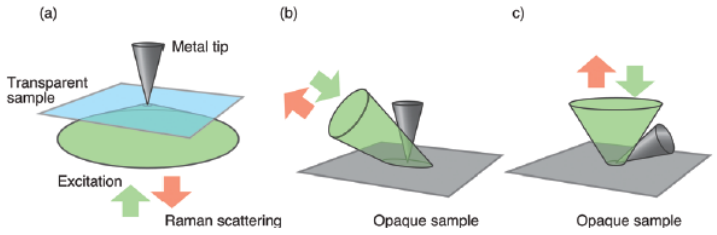

Figure 1.12: Different TERS configurations. Bottom up (a), side (B) and top (C) [46].

1.6.2 Configurations

There are three different configurations possible for TERS: Bottom illumination, Side illumination and Top illumination, see Figure 1.12 for images of each configuration. Each configuration has its own advantages and disadvantages depending on the sample in question. The substrate must be transparent in the bottom illumination, and the objective lens should have a high numerical aperture (NA). Radially polarized light is recommended for a tighter focus, resulting in a stronger beam. Side illumination uses linearly polarized light and a low NA objective. The parallel polarization of light causes a strong EM enhancement even with the low NA. Lastly, top illumination has the laser focused on the tip apex for maximum EM enhancement with a high NA objective [45]

1.6.3 Importance of TERS Tips

The TERS tip is a fundamental part of the enhancement process and is its distinguishing feature. Enhancement of the signal is achieved by exciting the surface plasmons of the metallic tip. This excitation can vary based on the electric properties of the metal, size and shape of the tip and also the set-up position [36]. The type of metal chosen depends on a variety of factors. The most common metals chosen are silver and gold. Silver is thought to be the best choice because the imaginary part of the

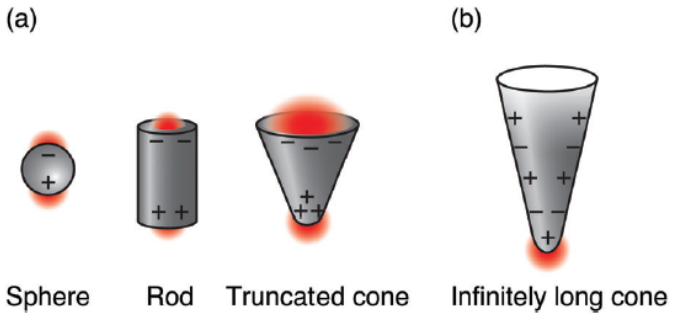

Figure 1.13: Different types of TERS tips showing hot spots for each tip [46].

dielectric constant is small, and its absorption peak is in the visible range of the spectrum. Gold tips are softer than silver and have lower signal enhancements but cannot be oxidized, prolonging its life.

Several different tip shapes can be fabricated, and the two main groups are Antenna-structured tips and sharpened tips (indefinitely long cone), as seen in Fig 1.13. Within the Antenna-structured tips, there are sphere, rod, and truncated cone tips [46]. Antenna-structured tips are fabricated by vacuum depositing an active metal on dielectric AFM cantilevers using thermal evaporation or sputtering. The nanospheres cover the tips making the cantilever plasmonically active. A downside to this method is that the vacuum can cause the cantilever to be distorted, rendering the AFM tip unusable [39]. Other methods of fabricating TERS tips are electron beam evaporation and sputtering. These techniques lead to uneven coating, low reproducibility, and a higher chance of being nonactive [46]. Electrochemical etching is another popular method of producing TERS tips.

Tip preservation is another important component of choosing a suitable tip. As mentioned above, silver is easily oxidized and can lose plasmonic activity in just a couple of days, but storing it in an inert environment with flowing nitrogen can prolong the activity by months. Coating the silver in aluminum oxide was also found to help preserve the tip while having a low impact on enhancement. Gold tips do not have

this problem, but given that they are softer than silver, they are easily destroyed and need an adhesion layer to keep the gold on the silicon tips [46].

1.7 Utilization for the Retina

Using the methods described above, we can analyze mice retina samples to determine the vitamin A concentration. The TERS data will allow us to look at the topography of the samples and the chemical map simultaneously with high accuracy. We also know from previous work [47] that conventional Raman is not powerful enough to overcome fluorescence and identify peaks. Having Raman data for each point of the AFM image allows us to identify areas of higher concentration and how they correlate to the height of the sample. We can also identify different structures within the sample, such as the macula, and determine the components within that area.

AFM data also allows us to find mechanical properties such as elasticity. Knowing the stiffness of the sample can also be important when analyzing samples with diseases. A force map can be done after the TERS data and overlaid to determine the sample's stiffness, height, and composition. This would be particularly useful for any disease that affects tissue structure, such as glaucoma.

Chapter 2

Computational Studies in support of TERS measurements

This chapter provides details on the input and output of the computational work carried out for this thesis and the Raman spectra completed. This section aims to help with the analysis for future TERS data of retinal tissues. Having computational spectra of vitamin A and its derivatives can help identify and confirm the composition of the tissues without having to complete Raman of standards, saving time and costs of materials.

2.1 Input

To calculate the Raman spectra, a molecule was created in Avogadro [48] and an NWChem [49] file was created. This file was copied to a file in WinSCP. A .sh file was created, and the simulation can start. When finished, the output file is downloaded and opened in Avogadro. If any of the vibrations are imaginary, then the simulation is done again; if not, the new coordinates are copied, and a new .nw file is created

to simulate the Raman spectra. A more detailed explanation of the process can be found in Appendix B. The parameters for each calculation is as follows:

- Theory: DFT
- basis set: 6-31+G*
- DFT Functional: b3lyp
- multi 1
- hessian thresh 1e-6

Each parameter was chosen because other papers looking at computational spectra of β-carotene (a compound structurally similar to those in question) use these parameters and reported sufficient findings [50, 51]. DFT theory has been used successfully in these papers for molecules of this size and similar functional groups. The basis set is large and provides reproducible and fairly accurate wavenumbers, so it is also a good starting point [52]. Once the calculations are complete, it can be decided if more precise data is needed. If so, a larger basis set can be tried. A larger basis set was not used in this experiment because our Raman shift values align well with reported literature shifts, as seen in Table 1.1 [11, 26]. The multiplicity is 1 because we are not considering radicals or non-singlet excited states as there is no evidence for this in vibrational excitations of these molecules. The threshold for convergence in the hessian is sufficiently low while still allowing for convergence, and is a typical threshold.

After each frequency calculation was completed, there were no imaginary frequencies, indicating that a minimum was found [52]. Using a smaller basis set than the one used in the experiment may lower the energy minimum, but the data collected

was in line with the reported data, which is sufficient for the purpose of collecting these spectra [52].

A sample input file for retinol is as follows:

```
echo
start molecule
title "Title"
charge 0
geometry units angstroms print xyz autosym
   C       -0.20293        5.66512       -1.16965
  ...
   H        2.62857        0.15089        0.33872
end
basis
  * library 6-31G*
end
dft
  xc b3lyp
  mult 1
end
task dft optimize
task dft freq
```

The cartesian coordinates used for the Raman vibration calculation are omitted above (...) and are given in Table B.1. Structures can be seen in Figure 1.5, 1.7. All spectra are simulated with a laser excitation wavelength of 633 nm.

2.2 Analysis

Raman peaks and vibrations were visualized by uploading the molecule.normal file to Avogadro [48] and matching peaks from literature to the computed spectra. The peak of interest was chosen, and an animation based on the vibrational analysis tables in the output file showed the corresponding vibration. For example, the peak around 1650 cm^{-1} for 5,6-epoxyretinol was chosen, and the corresponding C=C bonds stretched within the simulation, indicating that this is the stretch that occurs at this wavenumber shift.

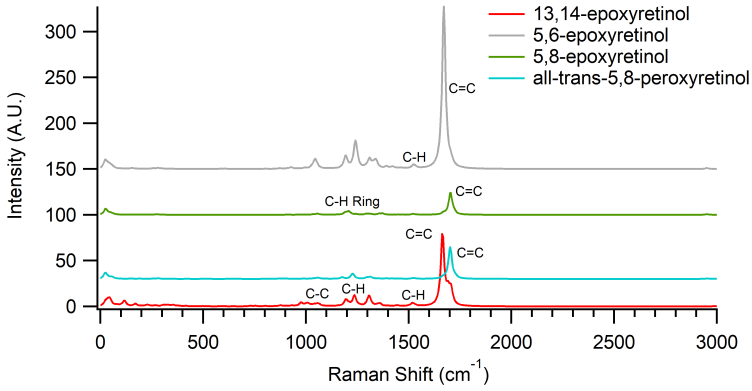

Figure 2.1: Computational Raman spectra of 13,14-epoxyretinol, 5,6-epoxyretinol, 5,8-epoxyretinol and all-trans-5,8-peroxyretinol. Similar peaks can be seen between 1000 cm^{-1} and 1700 cm^{-1}. 13,14-epoxyretinol and 5,6-epoxyretinol have similar spectrum and 5,8-epoxyretinol and all-trans-5,8-peroxyretinol have a similar spectrum.

Raman spectra of various compounds related to vitamin A were simulated to identify peaks of interest and confirm any experimental data. Table 2.1 summarizes the analysis below. See Figures 2.1 2.2, 2.3, 2.4 and 2.5 for Raman spectra of each compound.

All of the compounds that had Raman spectra simulated had the same mode located around 1650 cm^{-1}, the C=C stretch in the chain of the compound. Similarly, they all have the same C-H stretch, around 1500 cm^{-1}, involving the hydrogens on the

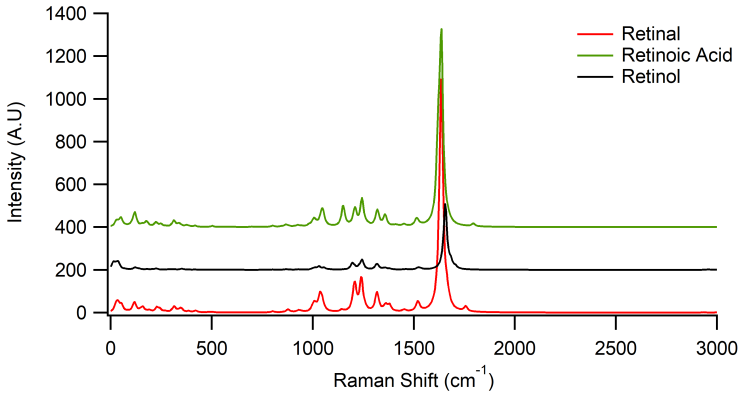

Figure 2.2: Computational Raman spectra of retinol, retinal and retinoic acid. Retinal and retinoic acid has the most similar peaks in comparison to retinol.

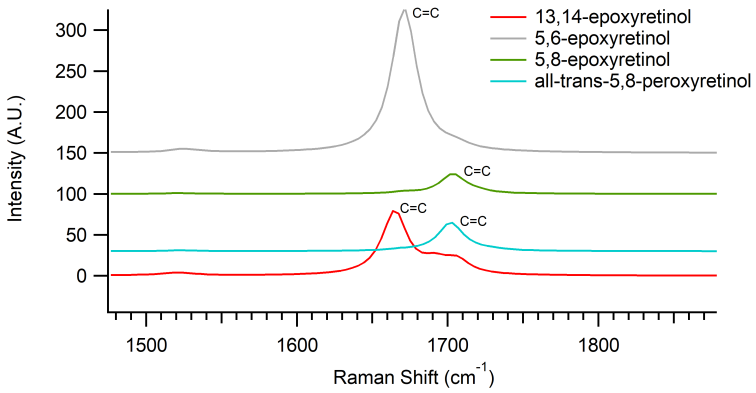

Figure 2.3: Computational Raman spectra of 13,14-epoxyretinol, 5,6-epoxyretinol, 5,8-epoxyretinol and all-trans-5,8-peroxyretinol zoomed in to about 1500 cm^{-1} to about 1850 cm^{-1}. 13,14-epoxyretinol and 5,6-epoxyretinol share a similar peak at about 1650 cm^{-1}, a C=C peak. 5,8-epoxyretinol and all-trans-5,8-peroxyretinol share a peak at about 1700 cm^{-1}, also a C=C peak.

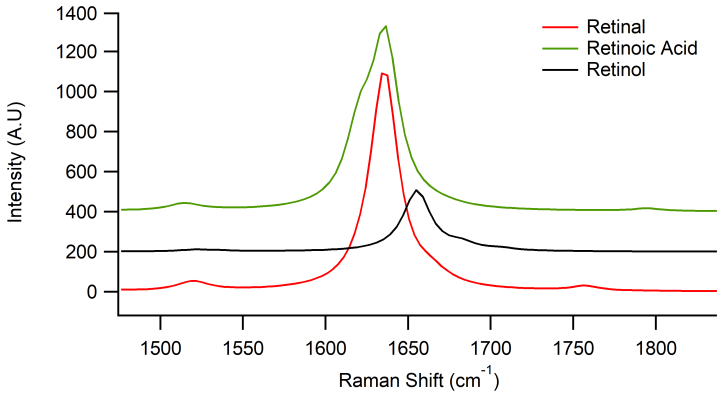

Figure 2.4: Computational Raman spectra of retinol, retinal and retinoic acid zoomed in at about 1500 cm^{-1} to about 1850 cm^{-1}. Here retinoic acid and retinal have a similar peak at about 1625 cm^{-1}, a C=C peak. Retinols C=C peak it at about 1650 cm^{-1}.

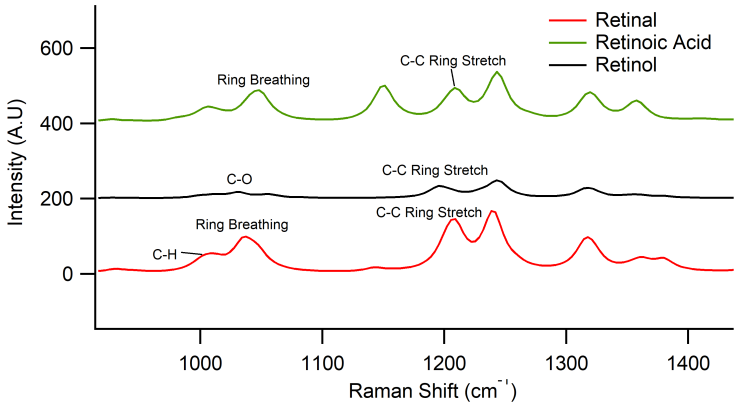

Figure 2.5: Computational Raman spectra of retinol, retinal and retinoic acid zoomed in at about 1000 cm^{-1} to about 1400 cm^{-1}. Retinol has a few similar peaks to retinoic acid and retinal. Retinal and retinoic acid have the most peaks in common. See Table 2.1 for detailed list.

ring and the chain. A common stretch seen in retinol, retinal and retinoic acid is the ring breathing stretch around 1080 cm^{-1}, with corresponding stretches of hydrogens of the CH_3 groups and the carbons. Also, the compounds have a similar C-C stretch of the ring, around 1200 cm^{-1}.

Retinol has one other stretch at 1091 cm^{-1}, a ring breathing stretch. Retinoic acid has a C-H stretch at 1409 cm^{-1}, which is the stretching of the CH_3 group of the ring. It also has a CH_3-C stretch at 1439 cm^{-1}. Finally, the carboxylic acid group stretch is located at 1794 cm^{-1}. Retinal has a stretch at 1047 cm^{-1}, mainly a C-H stretch, but also has some C-C stretches in the ring and the chain. It has another C-C ring stretch at 1201 cm^{-1}, and the aldehyde stretch is at 1758 cm^{-1}, similar to the carboxylic acid stretch in retinoic acid.

For the retinol-related compounds, all-trans-5,8-peroxyretinol has a peak at 1054 cm^{-1}, which is the C-O stretch of the alcohol group. 13,14-epoxyretinol has a C-H stretch at 1260 cm^{-1}. 5,6-epoxyretinol has a CH_3 stretch on the ring portion of the compound. Finally, 5,8-epoxyretinol has a C-H ring stretch at 1236 cm^{-1} and another C-H stretch at 1312 cm^{-1}.

Table 2.1: Band Assignments for the Simulated Raman Spectra

Compound	Wavenumber (cm^{-1})	Assignment
Retinol	1088	C-O Alcohol stretch
Retinol	1091	Ring Breathing
Retinol	1212	C-C Ring stretch
Retinol	1541	C-H
Retinol	1638	C=C

continued on next page

Continuation of Table 2.1

Compound	Wavenumber (cm^{-1})	Assignment
Retinoic Acid	1085	Ring Breathing
Retinoic Acid	1211	C-C Ring stretch
Retinoic Acid	1409	C-H
Retinoic Acid	1439	CH_3-C
Retinoic Acid	1527	C-H
Retinoic Acid	1664	C=C
Retinoic Acid	1794	Carboxylic acid group stretch
Retinal	1077	Ring Breathing
Retinal	1047	C-H
Retinal	1201	C-C Ring stretch
Retinal	1503	C-H
Retinal	1624	C=C
Retinal	1758	C=O Aldehyde Stretch
All-trans-5,8-peroxyretinol	1054	C-O
All-trans-5,8-peroxyretinol	1537	C-H
All-trans-5,8-peroxyretinol	1667	C=C
13,14-epoxyretinol	1066	C-C
13,14-epoxyretinol	1260	C-H
13,14-epoxyretinol	1533	C-H
13,14-epoxyretinol	1653	C=C
5,6-epoxyretinol	1547	C-H
5,6-epoxyretinol	1671	C=C
5,6-epoxyretinol	1438	CH_3 Ring

continued on next page

Continuation of Table 2.1

Compound	Wavenumber (cm^{-1})	Assignment
5,8-epoxyretinol	1091	C-C Ring
5,8-epoxyretinol	1236	C-H Ring
5,8-epoxyretinol	1312	C-H
5,8-epoxyretinol	1511	C-H
5,8-epoxyretinol	1669	C=C

End of Table 2.1

2.3 Conclusions

This analysis can help with identifying peaks in the tissues during the experiment. Knowing the approximate location of certain bonds in all of these compounds will help identify peaks when doing spectra of actual tissues. Having spectra of possible derivatives that can form in light and air will also help distinguish the peaks. We can take the spectra of the tissues and superimpose these spectra to compare similar peaks, and we can take all the common peaks and sort through them to help identify all the compounds in the sample.

However, the simulated spectra are done in a vacuum which is not how the experiment will be carried out. Calculations done in a vacuum will not have any intermolecular interactions, which will cause the Raman shifts to be different in a calculation than in the tissue. Other compounds in the tissues will be interacting with the molecule of interest, causing the bonds to stretch or bend in other ways. This will impact how much energy they absorb and how it scatters the photons, resulting in the different Raman shifts. The real tissue spectra will also contain peaks from non-retinol-related compounds such as lipids and sugars, which may have some fluorescence. This will

also impact the spectra and the position of the peaks. Keeping in mind that the calculations are for a single molecule and that the actual results will not precisely match the computed spectra or some of the literature values, these calculations still provide a significant and necessary starting point.

Part II:

Force Spectroscopy of Collagen Matrices

Chapter 3

Collagen

3.1 Motivation

Collagen matrix impacts cell behaviour [53]. It was found that changing the collagen overlay can affect the secretion of adipokine from mature adipocytes. The two different collagen overlays tested were PBS and HANKS collagen. The PBS collage suppressed the leptin more than the adiponectin, whereas the HANKS suppressed both adipokines. Changing the stiffness of the matrix also has an impact on the cell behaviour [54]. It was found that studying samples on a hard surface such as glass/plastic can impact the expression in endothelial cells.

Since we know that biological tissues usually have a change in mechanical properties when probed on different length scales, we can fabricate AFM tips with varying radii and perform indentations to quantify the differences. A typical collagen matrix is made from many collagen fibrils that form a network. Using the various tips, we can see if there is a difference in Young's Modulus (elasticity) to examine if the samples become stiffer when probed with the smaller tip or softer when probed with the smaller tip.

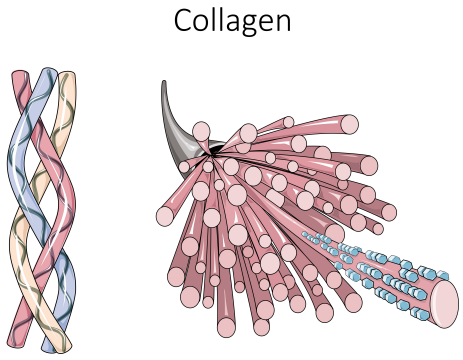

Figure 3.1: Collagen triple helix (Left). Fiber showing individual fibrils (right). Wikimedia Commons, license CC BY-SA 3.0, Laboratoires Servier.

3.2 Collagen

Collagen is the most abundant protein in the human body [55]. It is primarily located in the skin, bone, tendons, ligaments and the extracellular matrix [56]. There are a total of 28 types of collagen but we are interested in type I.

3.2.1 Type I Collagen

The structure of collagen is a triple helix with three α chains. Each chain is 1000 amino acids long with the repeating structure of Gly-X-Y, where X and Y are usually proline and hydroxyproline but can be any amino acid [57] [56]. The three chains are held together via hydrogen bonds. The structure of the helix can be seen in Figure 3.1. Type I collagen has the ability to form highly oriented supramolecular aggregates [58]. They start as the triple helix and self-assemble to be side-by-side monomers. Then they come together to form microfibrils with diameters of 4-5 nm, then again to form larger fibrils. These molecules have a quarter-staggered array with diameters of 25-400 nm [59]. They end up as micrometer-sized fibers that form the tissues and organs. The pattern of the bands in type I collagen has a periodicity of

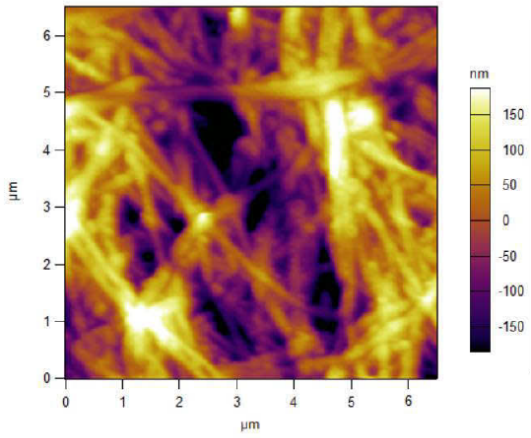

Figure 3.2: AFM image of collagen matrix (Zhe Dong) [60].

67 nm, see Figure 3.3 to see banding patterns.

Collagen fibrils in the tissues function to resist tensile forces; in bones, it provides stiffness and determines the load-bearing, tensile strength, and torsional stiffness [59].

Collagen samples studied in this thesis are a network of fibrils, as seen in Figure 3.2. Collagen fibrils are a common component of artificial extracellular matrices (ECM). Artificial ECMs are an essential component for cell culturing. They help regulate behavior, cell signaling and act as a physical barrier/cell scaffolding [60, 61]. They replicate natural ECMs that are present in vivo. ECMs in vivo are mostly comprised of interstitial matrix and the basement membrane; one artificial ECM uses fibril collagen and a protein complex extracted from the ECM of a tumor cell of a particular mouse [60].

3.3 Colloidal tips

First created by Ducker and Butt [62, 63], colloidal tips are a type of AFM tip with a smooth spherical tip instead of the conventional sharp AFM tip. [64] Colloidal tips allow a higher total force to be exerted on the sample, which increases sensitivity and

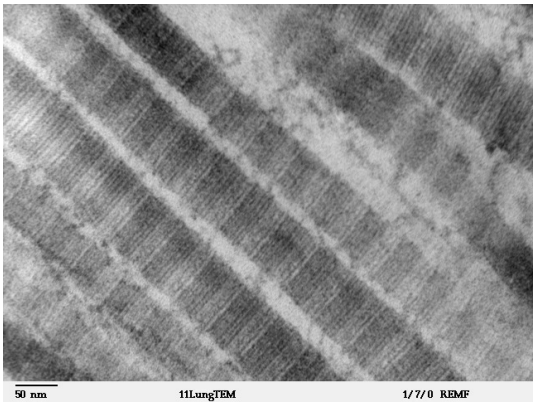

Figure 3.3: TEM image of type I collagen fibers in mammalian lung tissue. Louisa Howard, Public domain, via Wikimedia Commons

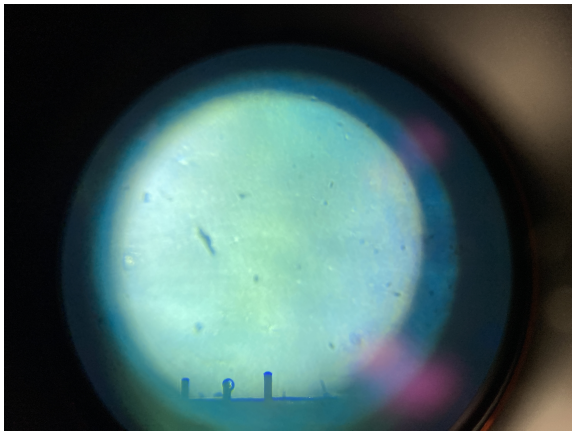

Figure 3.4: 45 μm colloidal tip prepared by AFM indentation.

force measurements can be analyzed more quantitatively due to the well-defined tip shape, see Section 3.4.5. This also decreases the likelihood of sample deformation or damage because of the lowered penetration depth. These tips are used for measuring adhesion, mechanical properties, or colloidal interaction forces [65]. They are typically made for silica or poly(styrene) and have diameters from 1-30 μm [66]. These tips can be customized with spheres of different radii and can be functionalized in many different ways. Given this, these tips are a great way to study mechanical forces on different length scales.

3.4 Experimental

3.4.1 Colloidal Tip Procedure

Colloidal tips have been made following the procedure from Zhe Dong, a previous master's student in the group [60]. See Figure 3.4 for an image of the cantilever. A summary of the procedure is as follows:

1. Dilute 44.5 μm polystyrene microspheres in water. The amount needed to dilute is dependant on the size of the microsphere.

2. Mount tipless cantilever into AFM; deposit microsphere solution onto silica wafer. Once dry, deposit glue on the silica wafer.

3. Use AFM indentation to apply glue onto cantilever. If too much glue is deposited, do another indentation on a clean surface.

4. Next, do an indentation over a microsphere. Let dry for a day.

5. Check sphere placement using microscope if not clear on AFM camera.

3.4.2 Collagen Matrices

The collagen matrix is formed by diluting type I Bovine collagen (Advance BioMatrix Lot 7088) with 1X PBS (Phosphate buffered saline) or 1X HANKS buffer solution to 3.3 mg/mL. This produces a PBS or HANKS matrix. Solutions were dropped on a glass slide and dried for at least 24 hours before use.

Another lab member made fibrils by bringing a 3.3 mg/mL suspension of collagen (Advance Biomatrix) in HCl(aq) up to pH 7 using NaOH(aq) and leaving the resulting suspension in the refrigerator. These are referred to as collagen fibrils throughout the thesis.

3.4.3 AFM Analysis and Calibration

All AFM force curves were obtained using an Asylum Research MFP-3D Atomic Force Microscope. The tips used were silicon tips with gold-chromium coated tips (CSC37/Cr-Au Micromash, USA), tipless silicon tips (NSC35/tipless/Cr-Au Micromash, USA) with polystyrene microspheres attached, and 5-9 μm colloidal tips (CPFM_SiO_2-A/Au/5 NT-MDT, Russia). The tips' resonance frequency and spring constant are 17 kHz and 0.3 N/m for the CSC37, 35 kHz and 0.2 N/m for NSC35 colloidal tip and 55kHz and 0.6 N/m for CPFM colloidal tip. These values were determined by the thermal noise method using the software available. All data was analyzed to determine Young's Moduli using procedures written by previous group members on the IGOR pro software ([67]).

Force curves were collected using the three different sized tips as stated above. The tips were calibrated by the thermal method first to determine the spring constant, and then a force curve was taken on glass. The trigger point was 20 nN and a velocity of 1.00 μm/s. Three curves were collected per spot, and approximately 200-500 curves were collected per sample per type of tip. For curves with dwell, the force was held constant for 2 seconds while the tip sat on the surface. p values were determined through statistical analysis of the data, and the differences between data data sets plotted below were determined to be significant with $p < 0.05$. Some force curves were collected with the assistance of WISE student Danielle Laing.

3.4.4 Force maps

Force maps of all three samples were done with the CSC37, NSC35, and CPFM tips. Each tip was calibrated prior to use by completing a force curve on glass with a velocity of 1.00 μm/s and a trigger point of 20 nN.

32 × 32 pixel force maps were completed using the tips stated above. Three areas of each of the samples were mapped. The velocity was 1.00 μm/s, and the trigger point was 20 nN. The Johnson-Kendall-Roberts (JKR) model [68] was used to analyze Young's Modulus (E).

3.4.5 JKR Model

All force curves completed are analyzed using the Johnson-Kendall-Roberts (JKR) model [68]. This model is used because it takes into account the adhesion between the tip and sample. The adhesive force can be found using the following equation,

$$F_p = \frac{-3}{2}\pi\gamma R \tag{3.1}$$

where γ is the work of adhesion and R is the contact radius of the indenter. Using this model, we can calculate the sample Young's modulus using the following equation,

$$E = \frac{-3F_p}{\sqrt{R}}(1-\nu_s^2)\left[\frac{3(\delta_0-\delta_{adh})}{1+4^{2/3}}\right]^{-3/2} \tag{3.2}$$

where E is the Young's Modulus, F_p is the force of adhesion, ν is the Poisson's ratio, which is considered to be 0.5 for all biological samples [69], and the δ_0 and δ_{adh} are the tip displacement at a force of 0 nN and maximum adhesion, respectively. See Figure 3.5 for the Standard Linear solid model used for creep and stress relaxation.

3.5 Results and Discussion

Each collagen sample had force curves taken with three different sized tips, point 10 nm radius tip, NSC35 22.5 μm radius sphere tip and CPFM 5-9 μm radius tip. Creep data was taken for each tip and sample, as well as force curves without creep. Force

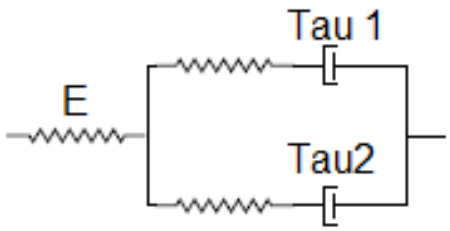

Figure 3.5: Standard linear solid model models the behaviour of viscoelastic material. This model predicts both creep and stress relaxation.

maps were acquired for each sample and tip without dwell time, as seen in Section 3.3.4.

Table 3.1: Manufacturer Name and Given name for each AFM tip

Manufacturer Name	**Given Name**
CSC36	Point
NSC35	Large Sphere
CPFM	Small Sphere

Figure 3.7 shows box plots of the E of collagen fibrils. The point tip showed an average E of 1375.9 MPa, while the creep data taken with the tip showed an average E of 4691.5 MPa. Similarly, the creep data for the Large Sphere tip had an E of 66.3 MPa, and the non-creep data had an average of 10.76 MPa. The Small Sphere tip showed the same pattern with creep data average of 318.6 MPa and a non-creep average E of 40.20 MPa.

From the data, we can see that the Large Sphere had the smallest E, then the Small Sphere, and finally, the point tip with the largest E. We also see that the force curves with dwell time have a much larger spread than those without, regardless of the tip used. We have a larger range with the force curves with dwell because of the plasticity of the sample. Plasticity is the non-reversible deformation of a material, which is the opposite of elasticity, a reversible deformation. The degree of the plasticity varies with each spot of the sample we indent, and this causes the E to vary. The E of the sample

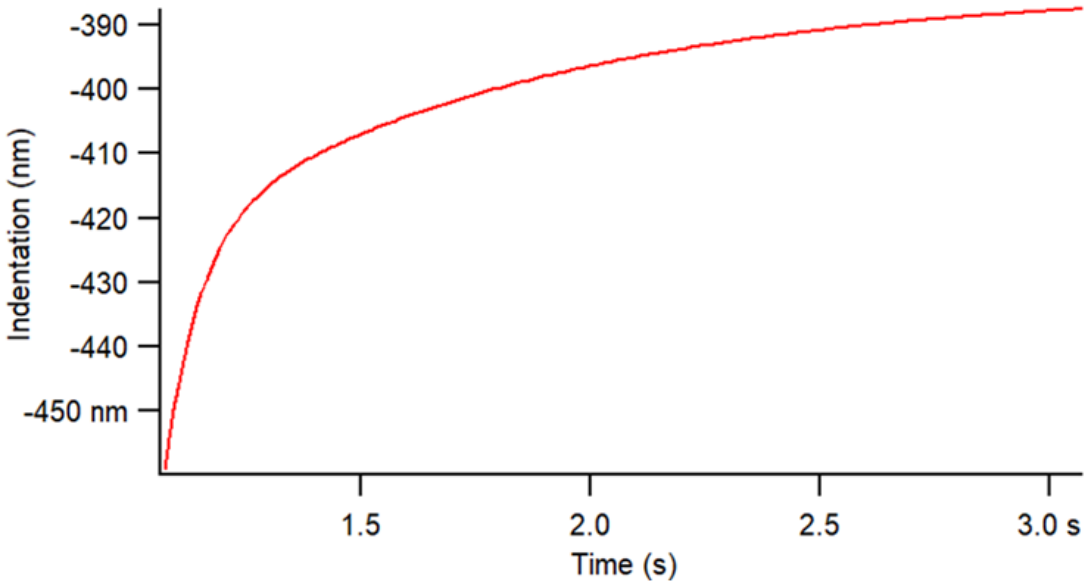

Figure 3.6: Example bi-exponential fit for calculating the creep characteristics.

found using the JKR model relies on the slope of the retract line of the force curve, and the plasticity changes the slope of this line and changes the E. The plasticity causes all the matrices to have an extensive range of deformations. Regarding creep characteristics, we see that in Figure 3.8 only one of the three tips used shows both negative and positive creep indentation. The sphere tips show only positive creep, both within the same range. Positive creep indentation indicated relaxation away from the tip and negative being relaxation towards the tip. The indentation occurs on the nm length scale.

For τ_1 and τ_2 creep characteristics, τ_1 is the short-term creep characteristic time and it is 63.4% of the time that the total creep indentation occurs. τ_2 is the long-term creep characteristic time and accounts for 36.6% of the remaining indentation. Each τ_1 and τ_2 have been fitted to a bi-exponential fit (see Figure 3.6 which best describes the data. Since we have a dwell time of only 2 s we can ignore the τ values above 2 s. Since the bi-exponential fit requires data beyond the time frame of the dwell, it is

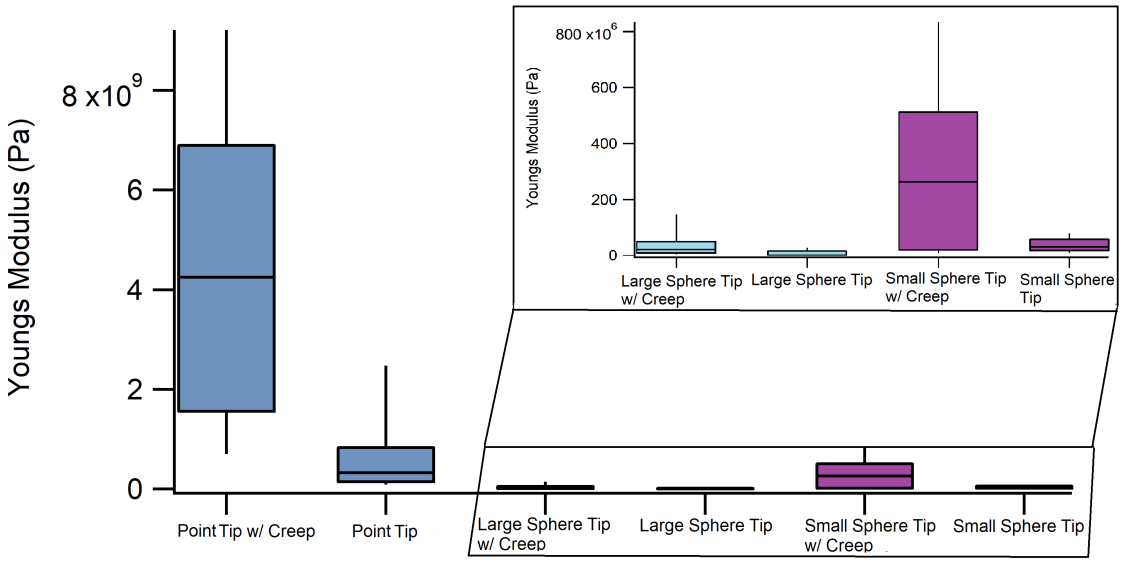

Figure 3.7: E of collagen fibrils. Point tip has highest E then Small Sphere tip and last the Large Sphere tip. Force curve retractions taken after a dwell time have a larger spread of values while the retractions taken immediately after indentation show a smaller spread.

therefore not valid. Those values are therefore meaningless.

The plots tell us three things: 1) we have two relaxation processes; 2) the sphere tips are better at resolving or capturing the two processes better than the point tip; and 3) the indentation of the network happens faster than the fibrils. We know the Large Sphere tip, in this case, resolves both processes better because the τ_1 for the Large Sphere is much smaller than the τ_2. The τ_1 and τ_2 graph can be seen in Figure 3.9. See Table 3.2 for creep indentation and $\tau_{1,2}$ averages.

The results for the PBS collagen are similar to those of the collagen fibrils. We see that the force curves with creep have a larger range of E and that the E is higher with the dwell time. Additionally, for the point tip, the E is 6800.3 MPa and with dwell it is 14135.2 MPa, more than double with dwell time. For the Large Sphere, the E is 21.734 MPa and with dwell it is 48.761 MPa and the Small Sphere tip the E is 221.155 MPa and 390.629 MPa with dwell, see Figure 3.10 for box and whisker

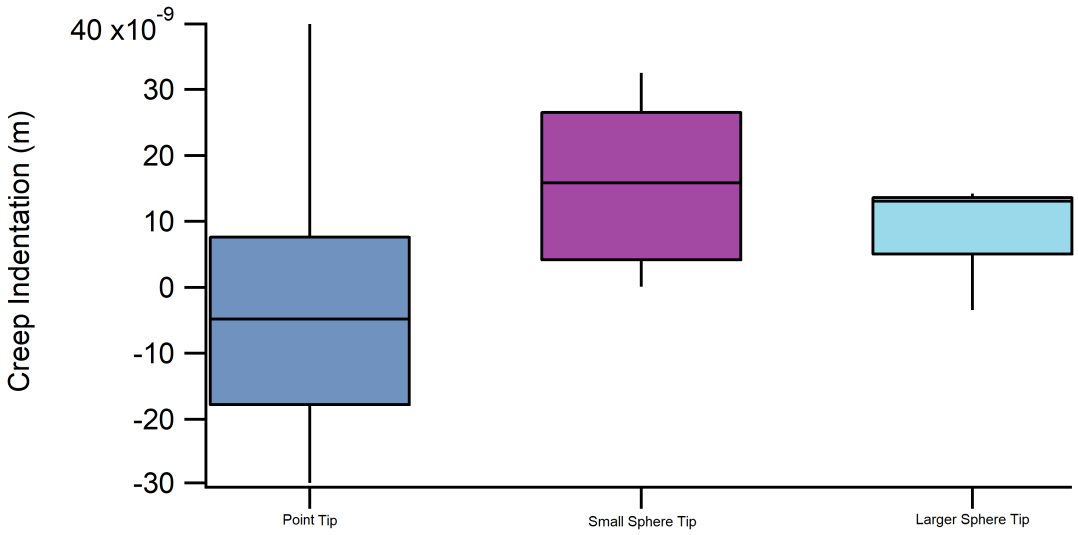

Figure 3.8: Creep indentation box and whisker plots for collage fibrils.

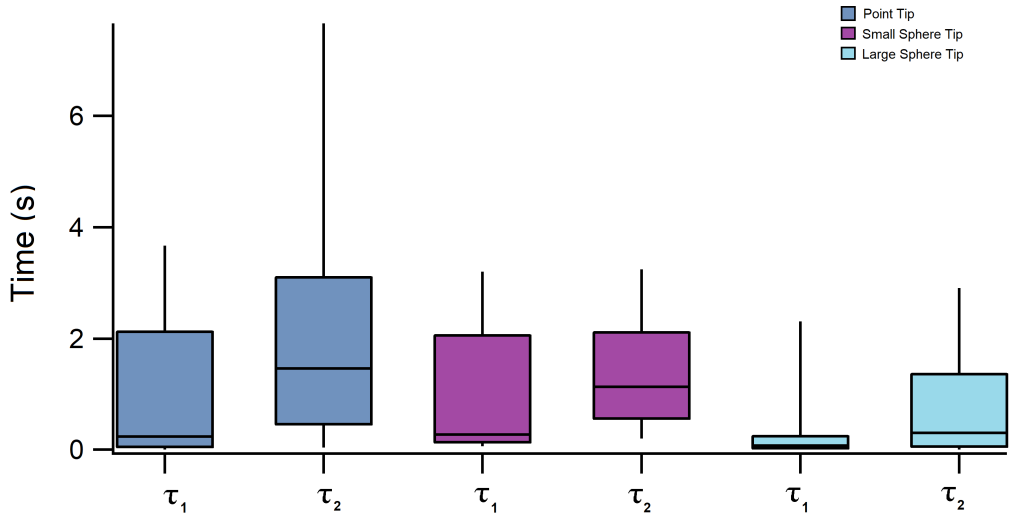

Figure 3.9: Box and whisker plots of τ_1 and τ_2 for three different tips for the collagen fibril sample.

Table 3.2: Young's moduli and creep characteristics of collagen.

Tip	**E (MPa)**	**Creep (nm)**	τ_1 **(s)**	τ_2 **(s)**
Point	1375.94 ± 4327.96	-	-	-
Point	4691.54 ± 3420.97	-4.022 ± 42.949	0.401 ± 0.532	0.888 ± 0.680
Large Sphere	10.75 ± 15.25	-	-	-
Large Sphere	66.30 ± 12.79	9.913 ± 24.958	0.380 ± 0.789	0.533 ± 0.710
Small Sphere	40.20 ± 27.07	-	-	-
Small Sphere	318.59 ± 305.82	18.023 ± 19.011	0.453 ± 0.587	0.987 ± 0.613

plot of results.

The creep indentation graph in Figure 3.11 shows all three tips with both negative and positive creep, all on the nm scale. The τ_1 and τ_2 graph in Figure 3.12 shows a similar trend as the fibrils in that there are two relaxation processes, and the spheres can resolve it better than the point tip. In this case, the Small Sphere can resolve both processes the best. See Table 3.3 for creep indentation averages and $\tau_{1,2}$.

Table 3.3: Young's moduli and creep characteristics of PBS collagen.

Tip	**E (MPa)**	**Creep (nm)**	τ_1 **(s)**	τ_2 **(s)**
Point	6800.3 ± 3965.80	-	-	-
Point	14135.2 ± 9553.72	-6.662 ± 14.625	0.333 ± 0.524	0.885 ± 0.628
Large Sphere	21.734 ± 18.58	-	-	-
Large Sphere	48.761 ± 50.17	-2.204 ±14.222	0.337 ± 0.585	0.824 ± 0.625
Small Sphere	221.155 ± 246.78	1.932 ± 10.313	0.314 ±0.580	0.820±0.746
Small Sphere	390.629 ± 229.21	-	-	-

As we have seen in the previous results, the results for the HANKS collagen follow a very similar pattern with one exception. The point tip shows the highest E, 10,203.1 MPa and 12063.6 MPa with dwell. The Large Sphere tip has an E of 79.91, the E with dwell is 24.37, and the Small Sphere tip has an E of 324.471 MPa and E of 600.959 MPa with dwell. All creep indentation results have a negative creep on the nm scale, see figure 3.14 for creep indentation graphs. We see that the τ_1 is smaller

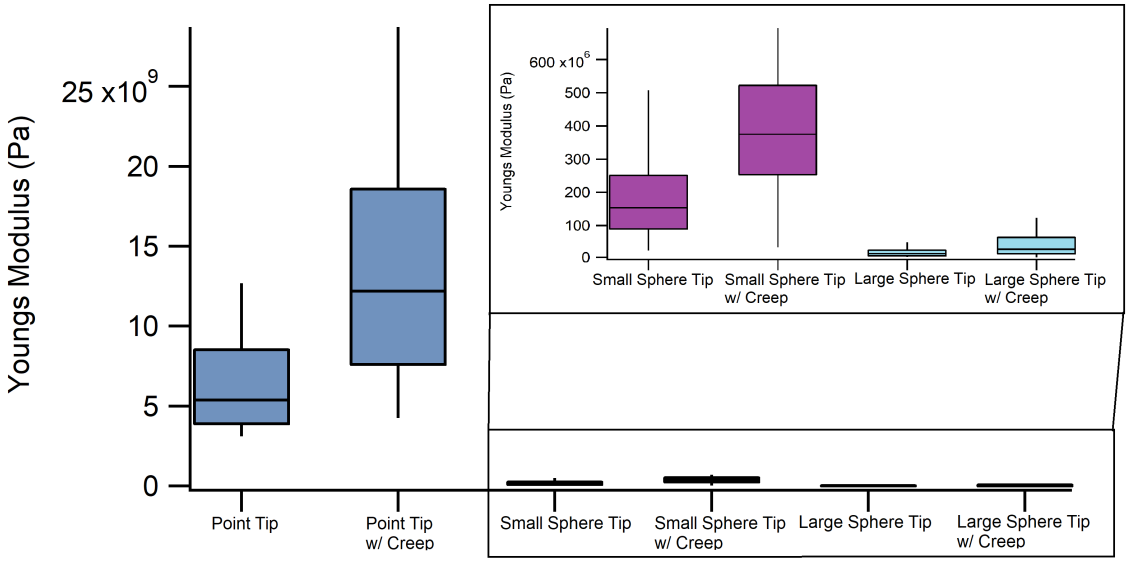

Figure 3.10: E of PBS collagen using three different tips with and without applying a dwell time. Point tip shows the highest E, then Small Sphere tip and then Large Sphere. Added dwell time increased spread of values.

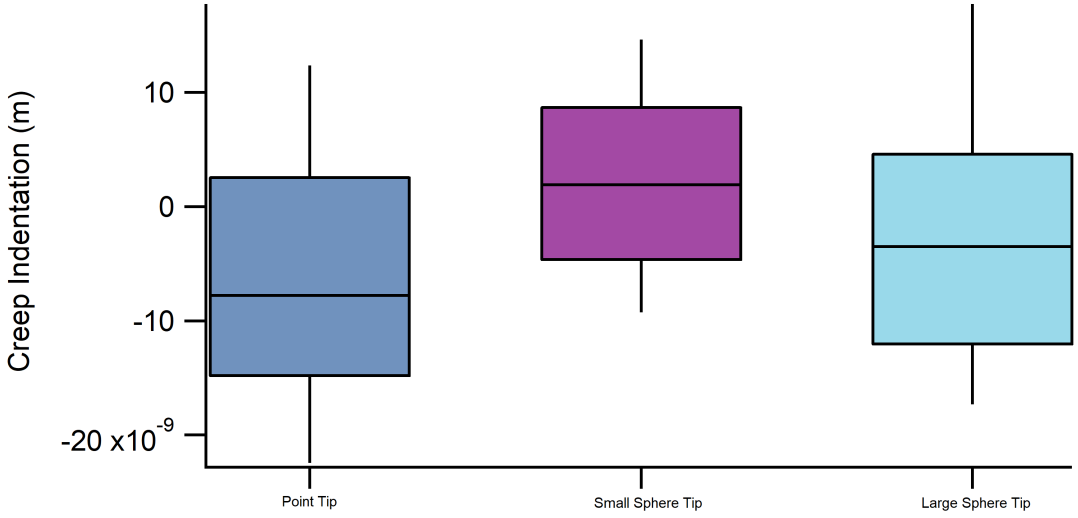

Figure 3.11: Creep indentation box and whisker plots for PBS collage.

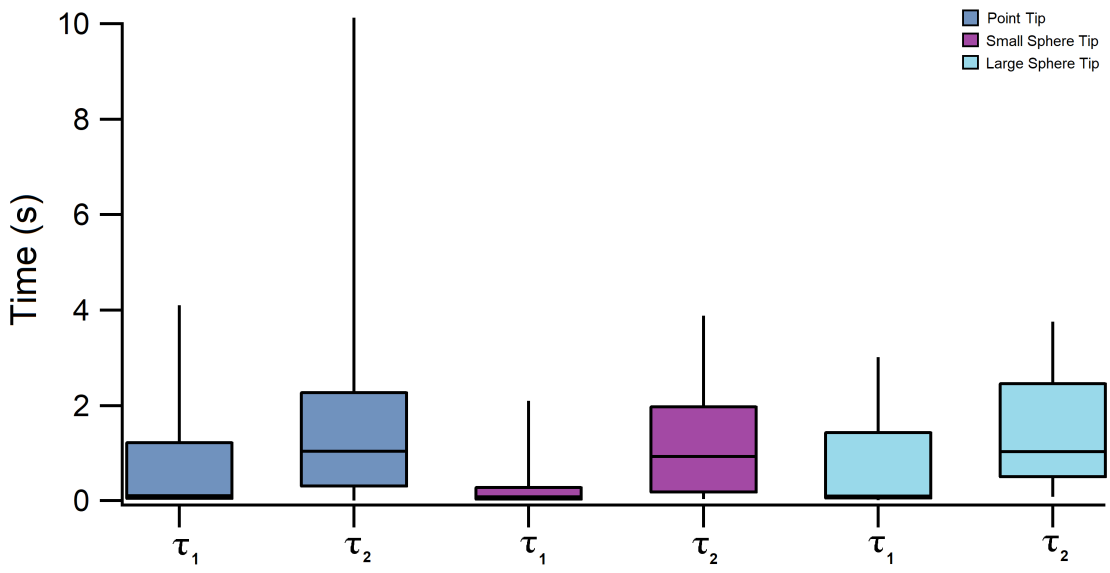

Figure 3.12: Box and whisker plots of τ_1 and τ_2 for three different tips for the PBS collagen sample.

than τ_2 for the sphere tips, meaning they can resolve the two relaxation processes the best, see Table 3.4 for creep indentation and $\tau_{1,2}$ averages, Figure 3.15 for $\tau_{1,2}$ graphs, and Figure 3.13 for box and whisker plots of E results.

Table 3.4: Young's moduli and creep characteristics of HANKS collagen.

Tip	**E (MPa)**	**Creep (nm)**	τ_1 **(s)**	τ_2 **(s)**
Point	10203.1 ± 6460.06	-	-	-
Point	12063.6 ± 5946.18	8.324 ±12.128	0.529±0.723	0.917±0.678
Large Sphere	79.91 ± 53.61	-	-	-
Large Sphere	24.37 ± 14.39	-2.204±12.261	0.152±0.429	0.825±0.850
Small Sphere	324.471 ± 219.86	-	-	-
Small Sphere	600.959 ± 433.17	-4.976±10.943	0.218±0.471	0.686±0.538

3.5.1 Force Maps

To get a sense for the local heterogeneity in force measurements, in addition to the many force curves analyzed above, I also measured force maps, sets of curves in close proximity to each other. Each force map contains a scale bar beside each height and

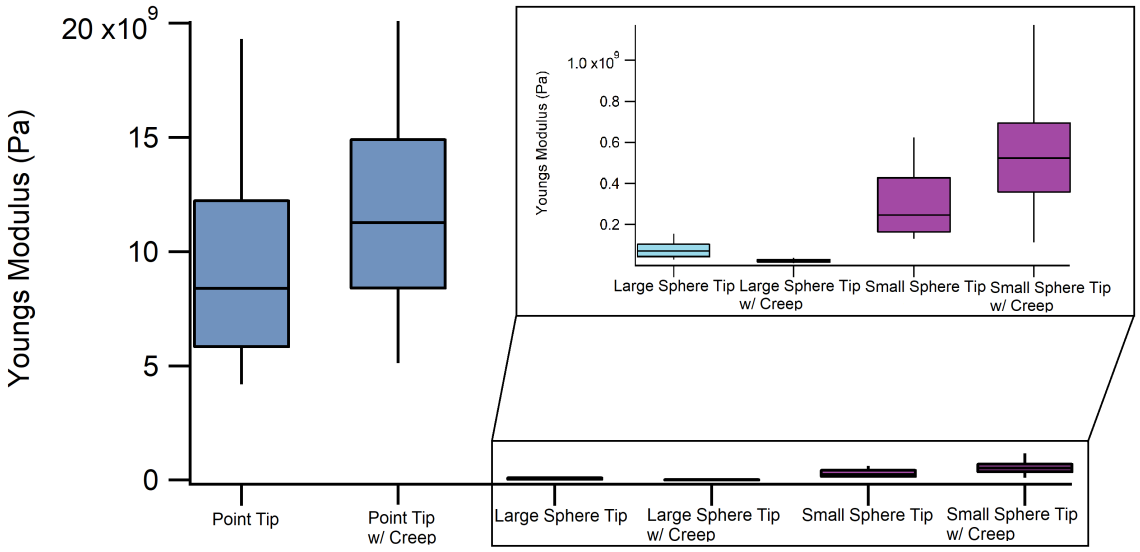

Figure 3.13: Box plots of E for HANKS collagen. Similarly to the previous collagen samples the E of the Point tip is the highest followed by Small Sphere tip an Large Sphere tip.

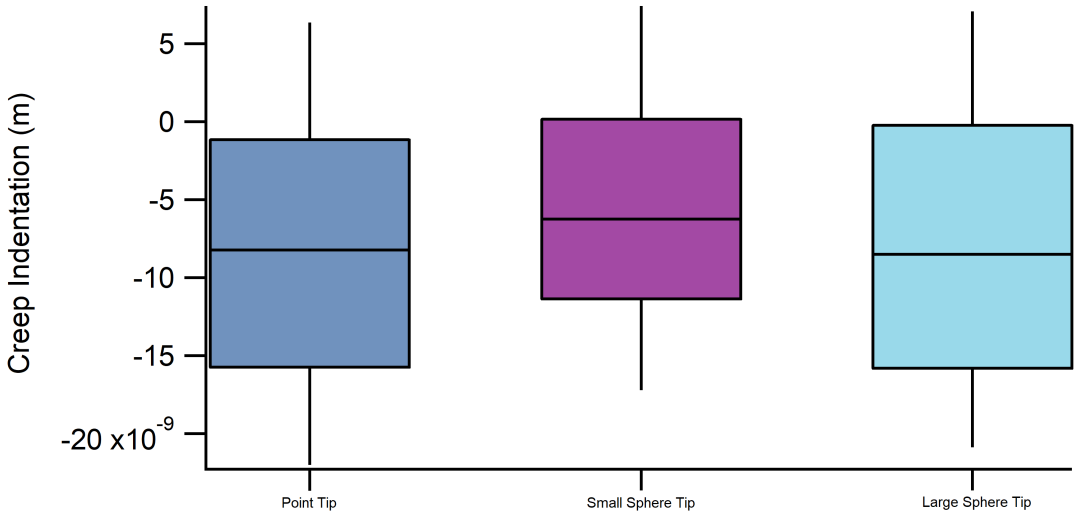

Figure 3.14: Creep indentation box and whisker plots for HANKS collage.

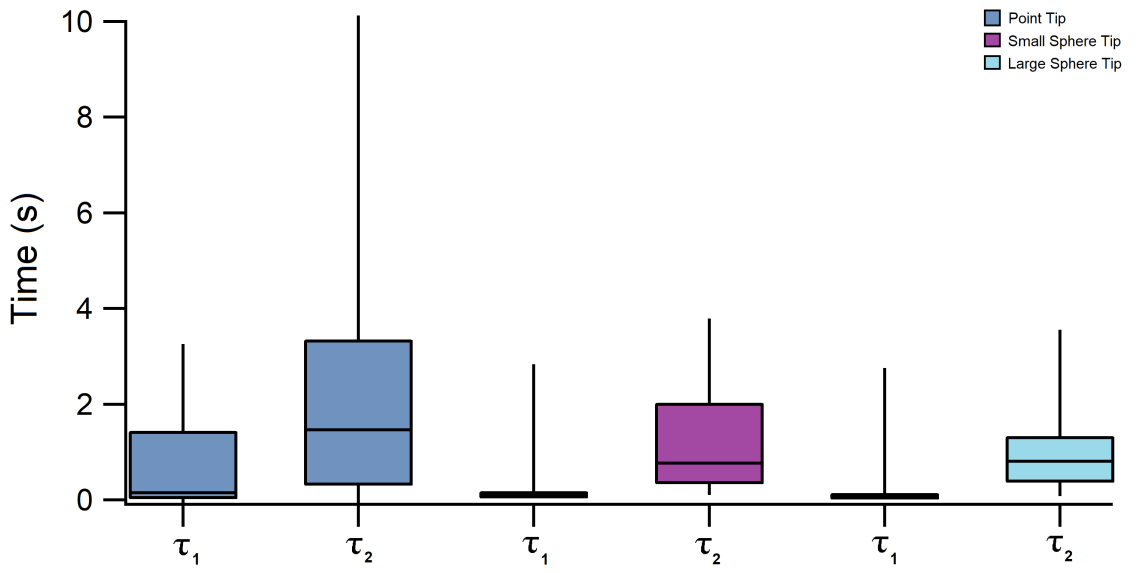

Figure 3.15: Box and whisker plots of τ_1 and τ_2 for three different tips for the HANKS collagen sample.

adhesion map. These bars represent the highest and lowest height and adhesion of the sample. The largest values are in yellow, and the lowest are in black. By looking at a representative map for each type of sample and tip (Figures 3.16, 3.17, 3.18, 3.19, 3.20, 3.21, 3.22, 3.23, and 3.24), we can see that is there is no correlation between height and adhesion, except in Figure 3.21 where there is a slight "halo" which matches the outline of the high feature in the height map.

For a sample that does have a relationship between these two you would see, for example, a high area would have either a large or small adhesion, and throughout the map we would see the same pattern. This indicates a potential for artifacts in our force curve data created by large jumps in the tip. A small amount of the data in Figure 3.21 does seem to be impacted by surface topography, but in Appendix A we can see that the rest of our force curve data, even that with even larger surface features such as in Figure A.7.

The average E for each map can be found in Table 3.5. Each sample and tip follows the same trend in E as the force curves in the results above, confirming that

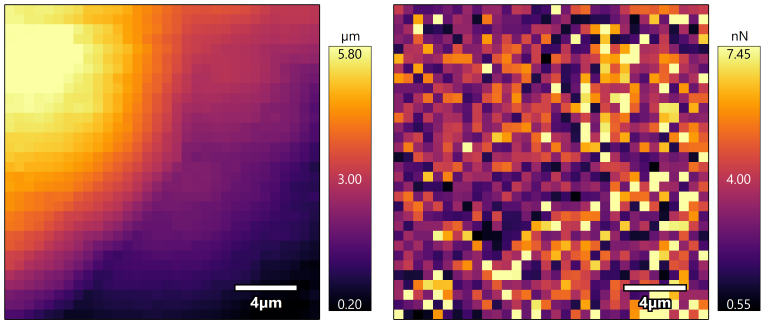

Figure 3.16: Height (left) and adhesion (right) maps taken on collagen fibrils using Large Sphere tip.

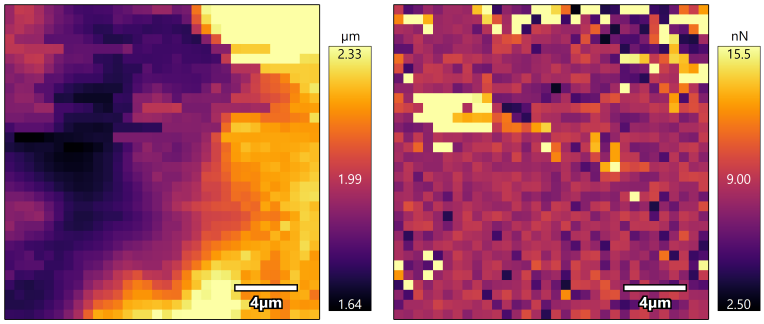

Figure 3.17: Height (left) and adhesion (right) maps taken on collagen fibrils using Small Sphere tip.

we have a good sampling of the surface at both short and long range.

Table 3.5: Average E of force maps with Varying tips (MPa)

Sample	**Point**	**Large Sphere**	**Small Sphere**
Collagen fibrils	951.81 ± 251.29	3.44 ± 1.43	551.52 ± 614.59
PBS Collagen	1794.26 ± 1176.68	35.60 ± 19.64	325.69 ± 174.23
HANKS Collagen	2334.57 ± 2253.95	4.83 ± 3.07	240.33 ± 115.92

3.6 Conclusions

In all three samples, HANKS, PBS, and fibrils, we see the same trend with E and the specific tip used. The point tip has the highest E, the Small Sphere tip with the

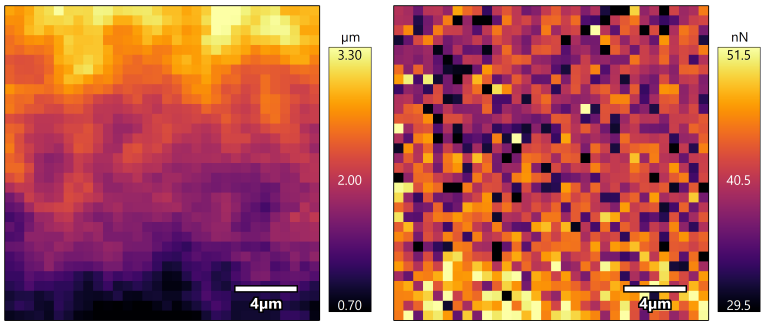

Figure 3.18: Height (left) and adhesion (right) maps taken on collagen fibrils using point tip.

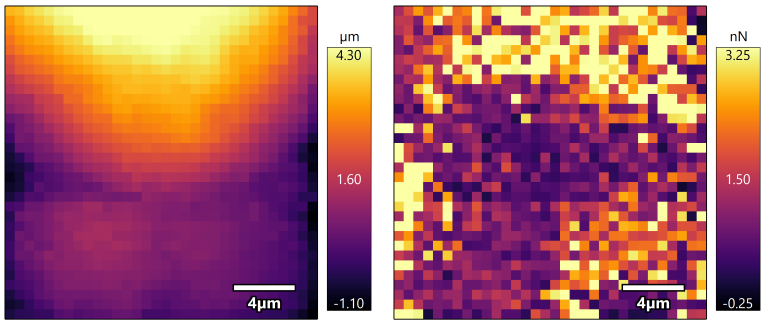

Figure 3.19: Height (left) and adhesion (right) maps taken on HANKS collagen using Large Sphere tip.

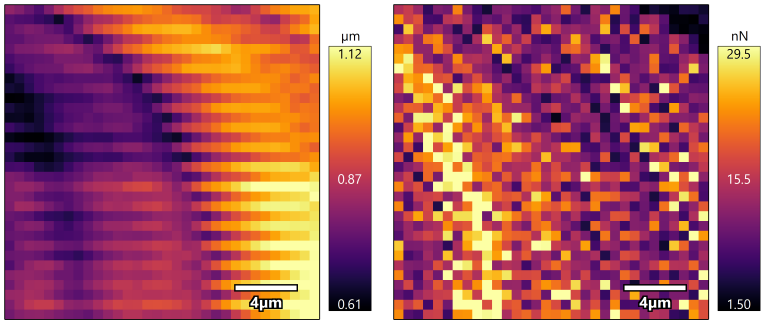

Figure 3.20: Height (left) and adhesion (right) maps taken on HANKS collagen using Small Sphere tip

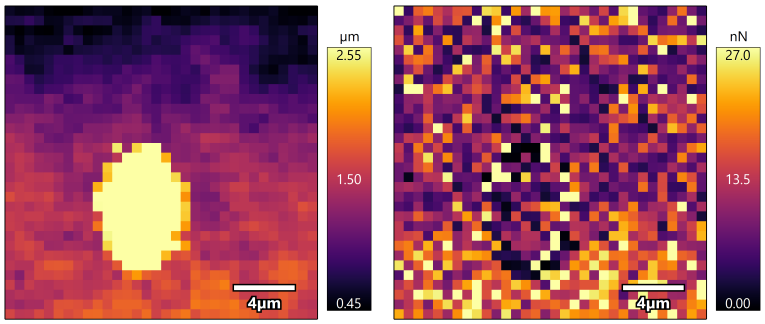

Figure 3.21: Height (left) and adhesion (right) maps taken on HANKS collagen using point tip

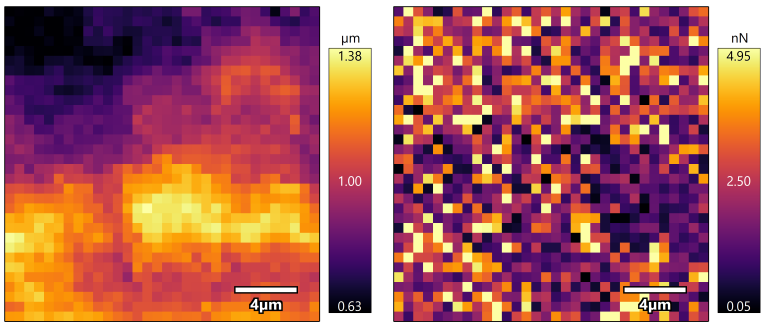

Figure 3.22: Height (left) and adhesion (right) maps taken on PBS collagen using Large Sphere tip.

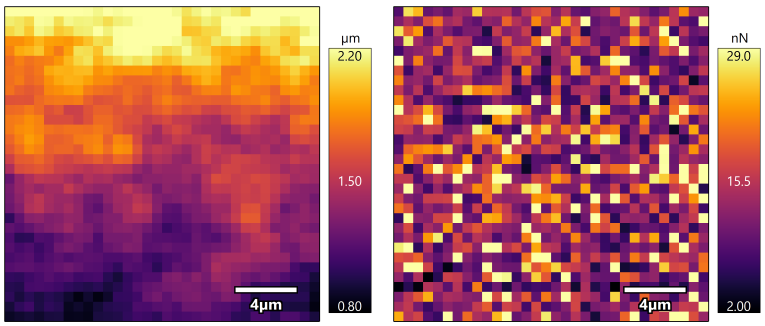

Figure 3.23: Height (left) and adhesion (right) maps taken on PBS collagen using Small Sphere tip

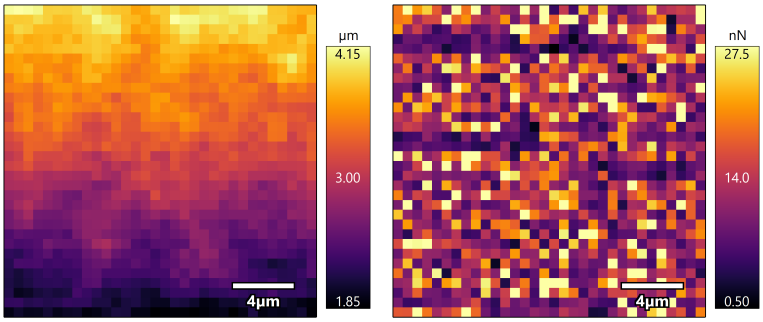

Figure 3.24: Height (left) and adhesion (right) maps taken on PBS collagen using point tip

next largest and the Large Sphere tip. This confirms the theory that tip radius and E are related; increasing the tip radius decreases the E. This may occur because of the difference in the network vs a single strand of collagen. The network comprises many strands of collagen, each overlapping and crossing each other, resulting in a network that can allow for more stretching. Point tip measurements show larger E, indicating stiffer fibrils since this indenter is not large enough to measure the network. Sphere tips show a small E making the collagen network much softer.

When comparing each tip and different samples, the Point Tip has the highest E for the HANKS collagen without dwell but with dwell, the PBS collagen has the highest E. The collagen fibrils have the lowest E for the point tip. The range between each sample is large, with the collagen fibrils' E being 1375 MPa without dwell and the next closest, 6800 MPa for PBS with creep. The Small Sphere tip has the highest E for PBS collagen without dwell and HANKS collagen with dwell; similarly, the collagen fibrils has the lowest for both, although the range in values over all three samples is much smaller than the point tip. Finally, for the Large Sphere tip, all values are relatively close, with the HANKS collagen having the highest E without dwell and collagen fibrils having the largest with dwell.

Creep indentation is consistent with each tip, with a few exceptions. The point tip

has a similar indentation with each sample besides the HANKS collage; this sample did not have a positive indentation. The Small Sphere tip has different magnitudes for each sample; HANKS collagen had no positive indentation, PBS collagen had both positive and negative, and the collagen fibrils just had positive indentation. Lastly, the Large Sphere tip also showed different indentations for each sample; again, the HANKS collagen had a negative creep, the PBS collagen had both positive and negative, and the collagen fibrils had positive creep but with the smallest range of any sample and tip. In all samples, we have seen indention on the nm scale.

Part III:

Conclusions

Chapter 4

Conclusions and Future Directions

4.1 Conclusions

The TERS work had to be put aside because of the pandemic, but my work lays the basis for future projects. I completed computational Raman spectra of vitamin A and its derivatives and photoproducts. Having this data will allow future students to easily confirm peak assignments or help distinguish the composition of the samples in question.

This is what we know about collagen matrices, thanks to my work. First, we have a working procedure on the fabrication of colloidal tips, which can be scaled to fit any size of colloid needed. As for the collagen membranes, we know that the tip radius of the colloidal tip changes the measured Young's Modulus (E) of the sample: smaller tip, larger measured E, larger tip, smaller measured E. We also know that the $\tau_{1,2}$ show two different relaxation processes. The spheres are the tips that can resolve these processes the best. With the HANKS and PBS membranes, it is the small sphere, and with the fibrils, it is the large sphere which works best. Based on the $\tau_{1,2}$, we can see that the network has a faster relaxation process, and the fibrils

are slower. The creep indentation of all the samples is relatively similar but does not follow any trends with either the tip or the sample matrix. We see a relaxation of the samples both towards and away from the tip and a slight overall creep indentation of the sample.

4.2 Future Directions

4.2.1 TERS

Future work on this project may include developing a working procedure to obtain TERS spectra on current systems in the lab. Completing TERS spectra of retinal tissues to determine the concentration of vitamin A in the tissue as a whole and its specific areas. Also, the possible combination of force spectroscopy with TERS to identify the concentration of vitamin A with the stiffness of the tissues. This can inform us of trends in the concentration and mechanical properties of the tissues and give further insight into retinal diseases [46].

4.2.2 Collagen Matrices

Possible future work that can be completed is confirming the results of this experiment on different samples, either biological or other materials. Cells can be cultured to examine the difference in E, creep indentation and $\tau_{1,2}$ for varying tip sizes to determine if the trends are repeated using different samples and tip sizes [70].

Part IV:

Appendices

Appendix A

Additional Force Maps

This appendix contains the additional force maps acquired during this project.

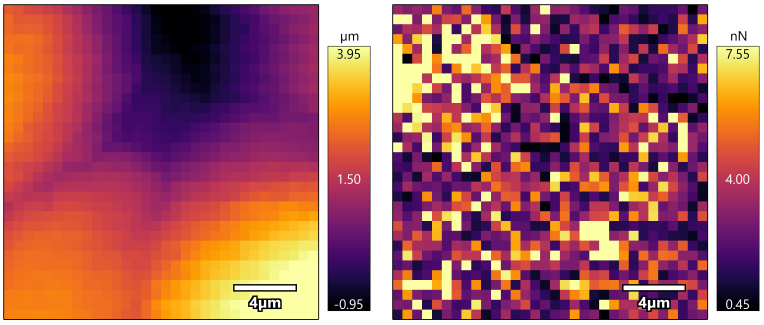

Figure A.1: Height (left) and adhesion (right) maps taken on collagen fibrils using Large Sphere tip.

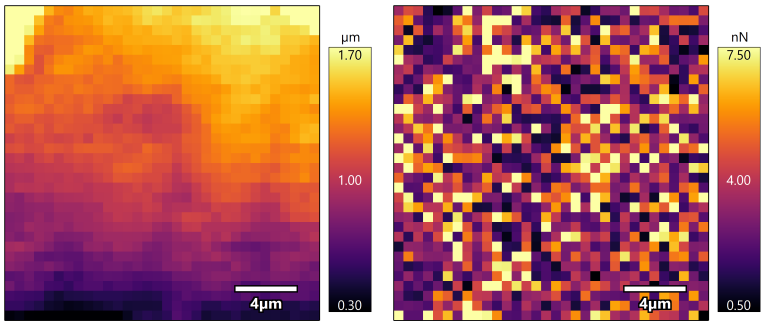

Figure A.2: Height (left) and adhesion (right) maps taken on collagen fibrils using Large Sphere tip.

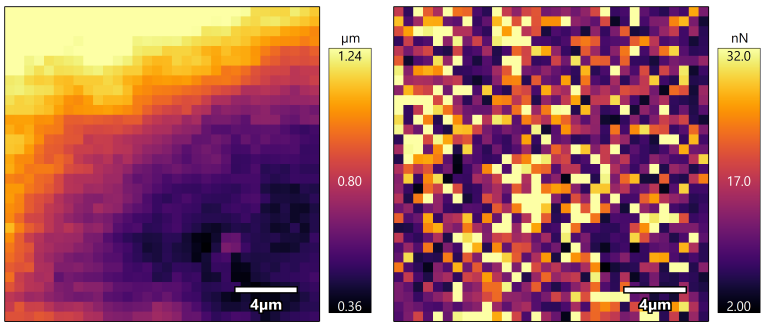

Figure A.3: Height (left) and adhesion (right) maps taken on collagen fibrils using Small Sphere tip.

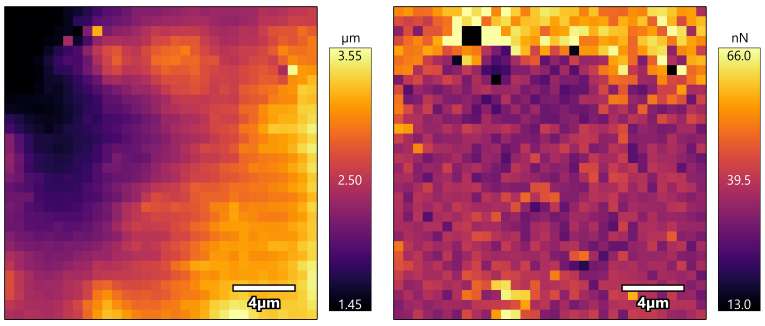

Figure A.4: Height (left) and adhesion (right) maps taken on collagen fibrils using point tip.

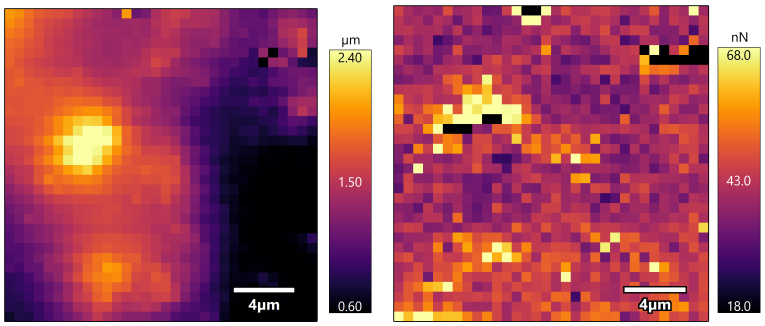

Figure A.5: Height (left) and adhesion (right) maps taken on collagen fibrils using point tip.

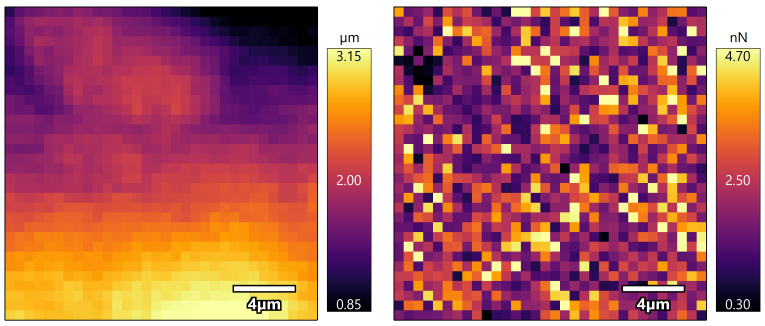

Figure A.6: Height (left) and adhesion (right) maps taken on HANKS collagen using Large Sphere tip.

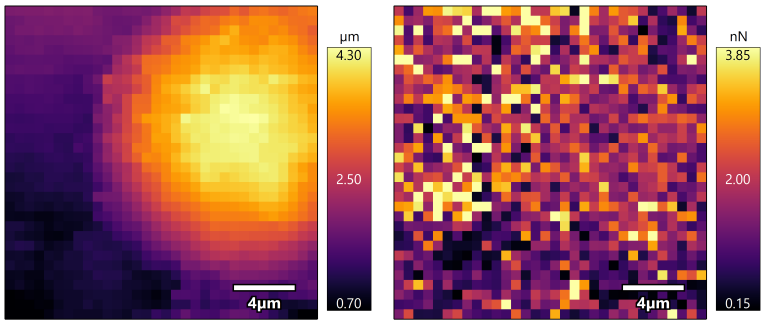

Figure A.7: Height (left) and adhesion (right) maps taken on HANKS collagen using Large Sphere tip.

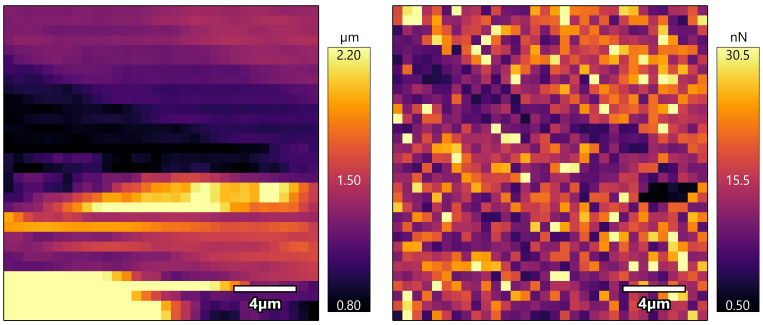

Figure A.8: Height (left) and adhesion (right) maps taken on HANKS collagen using Small Sphere tip

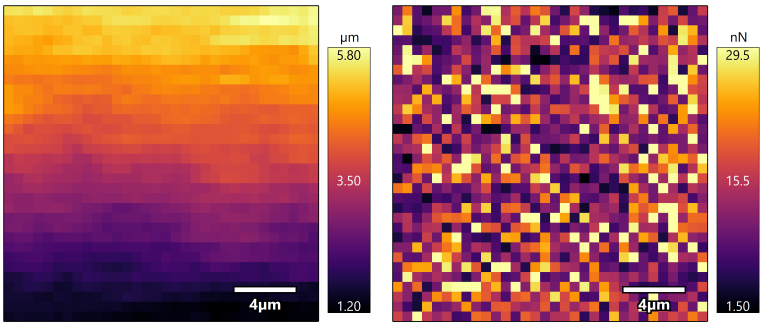

Figure A.9: Height (left) and adhesion (right) maps taken on HANKS collagen using Small Sphere tip

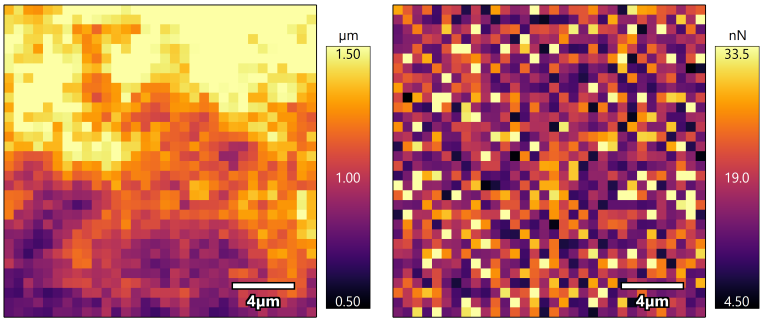

Figure A.10: Height (left) and adhesion (right) maps taken on HANKS collagen using point tip

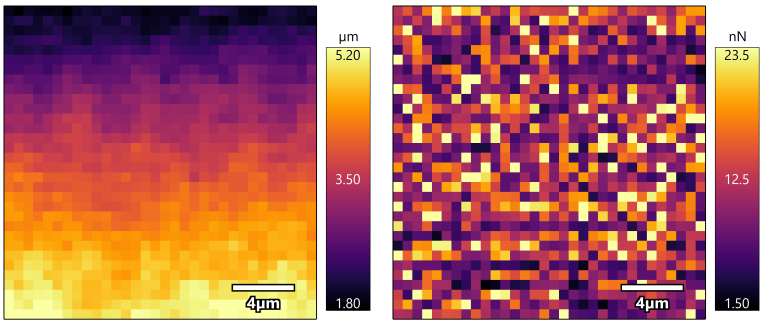

Figure A.11: Height (left) and adhesion (right) maps taken on HANKS collagen using point tip

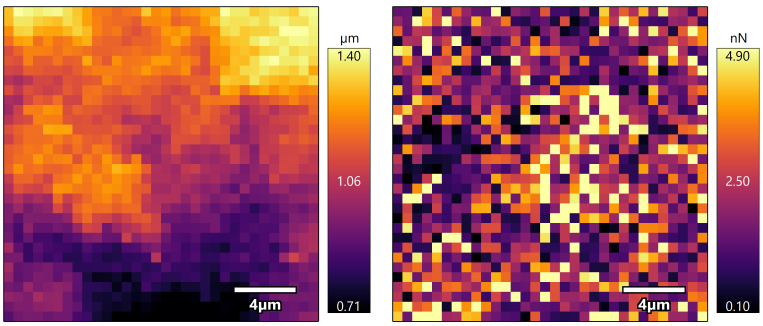

Figure A.12: Height (left) and adhesion (right) maps taken on PBS collagen using Large Sphere tip.

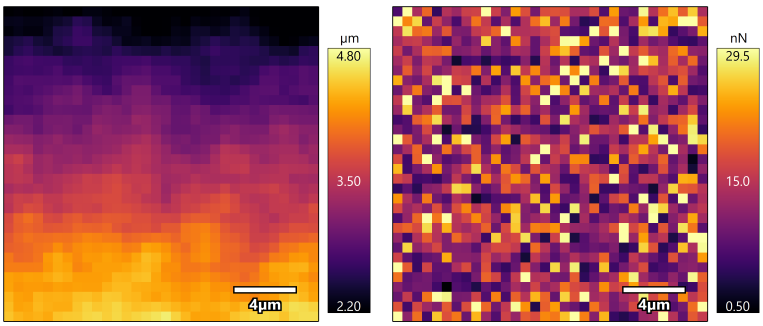

Figure A.13: Height (left) and adhesion (right) maps taken on PBS collagen using Small Sphere tip

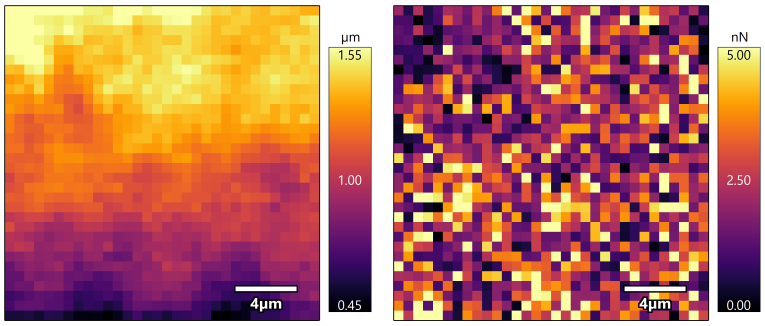

Figure A.14: Height (left) and adhesion (right) maps taken on PBS collagen using Small Sphere tip

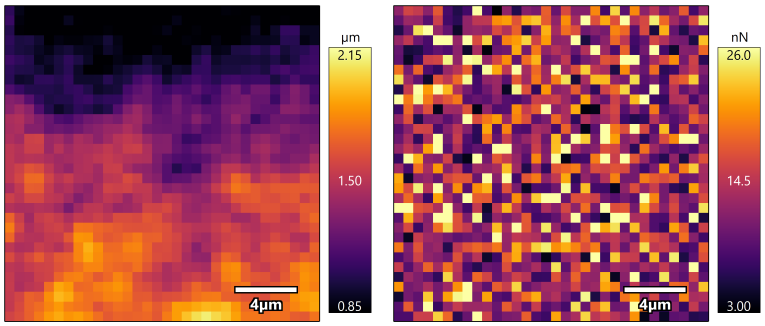

Figure A.15: Height (left) and adhesion (right) maps taken on PBS collagen using Small Sphere tip

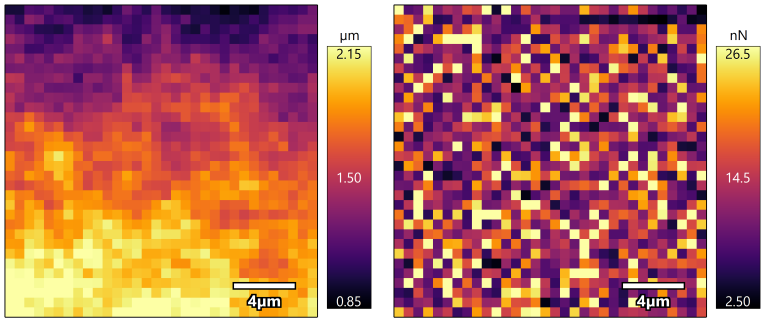

Figure A.16: Height (left) and adhesion (right) maps taken on PBS collagen using Point tip

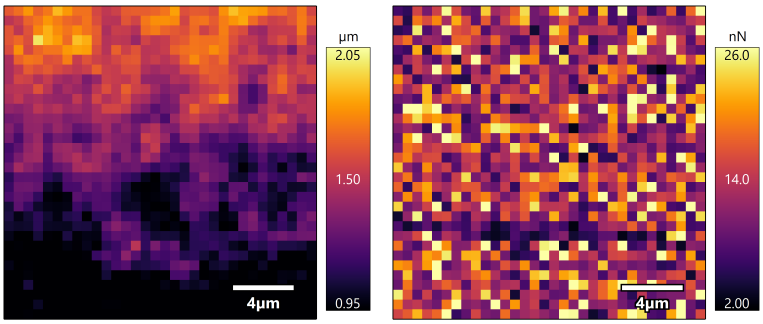

Figure A.17: Height (left) and adhesion (right) maps taken on PBS collagen using Point tip

Appendix B

Additional Computational Information

This appendix includes information on setting up computational calculations as well as some sample files [71].

The first step to completing a computational Raman spectrum is to make a molecule in Avogadro [48] and do an auto optimization to get the molecule close to the correct geometry as possible. You then create an .nw file with the calculation (in this case it would be geometry optimization), theory and basis set you are going to use. The .nw file also contains the initial xyz coordinates of the atoms to be optimized in angstroms. The input is created and you copy the resulting lines and create .nw file in WINSCP. In the last line of your .nw file you add the line "task dft freq". See sample input file for retinol below.

After this we create a .sh file which is a bash file. This is where we put the time we want the calculation to take and the memory or cpu we want to use. Once we run this file it creates an output file that contains all the information of the calculations completed. After the calculation is complete we upload the output file into Avogadro

and open the vibration tab. This tells us if the geometry optimization of the molecule needs to be completed again. If the vibrational table has a negative number in it the molecule is not in its stable form and needs to be optimized again.

Now that we have an optimized molecule we can do the Raman calculation. Still in Avogadro we create another .nw file and copy that to a a new .nw file in WINSCP. To this .nw file we add the Raman parameters such as the range of wavenumbers our spectra will contain as well as the wavelength of the laser you'd like to use. A new .sh file is created similar to the one above and you run the calculation once again.

To plot the spectra you download the molecule.normal file, load as a wave in Igor [67] and plot it in a graph.

A complete input file for retinol is as follows:

```
echo

start molecule

title "Title"
charge 0

geometry units angstroms print xyz autosym
   C       -0.20293        5.66512       -1.16965
   C        0.64078        4.50726       -0.56283
   C       -0.25014        3.43853        0.12134
   C       -1.57369        3.70064        0.41983
   C       -2.22772        5.03414        0.09340
   C       -1.23826        6.16096       -0.18490
   H       -2.86075        5.38157        0.93908
```

H	-2.89567	4.86745	-0.77957
H	-0.74409	6.48682	0.75265
H	-1.79138	7.03410	-0.59359
H	-0.75608	5.31351	-2.07116
H	0.46179	6.49598	-1.49380
C	0.42864	2.12771	0.41903
C	-0.15071	0.92052	0.26134
C	0.54371	-0.38396	0.49567
C	-0.14794	-1.51252	0.19608
C	1.95892	-0.38802	1.04085
C	0.33567	-2.91202	0.33552
C	-0.45138	-3.93448	-0.04703
C	-0.05681	-5.37215	0.04380
C	1.29435	-5.75306	0.61593
H	2.09866	-5.29149	0.00580
H	1.48031	-6.84451	0.63658
H	1.36978	-5.38413	1.66026
C	-0.94052	-6.29735	-0.39953
C	-0.69772	-7.78214	-0.38091
O	-1.81119	-8.44350	-0.91309
H	-0.54115	-8.10827	0.67127
H	0.19809	-8.00896	-1.00080
H	-1.60188	-9.41270	-0.87142
H	1.47988	2.16010	0.67281
H	-1.17036	0.87771	-0.10574
H	-1.15662	-1.39898	-0.19656

```
   H        1.31541       -3.12425        0.73403
   H       -1.43415       -3.70396       -0.45328
   H       -1.89480       -5.96284       -0.80132
   C       -2.50509        2.75564        1.15588
   H       -2.03761        1.85285        1.57859
   H       -3.35267        2.47097        0.49815
   H       -2.91245        3.27816        2.04709
   C        1.42749        3.88924       -1.74549
   H        0.73049        3.45858       -2.49684
   H        2.11209        3.08180       -1.41168
   H        2.05171        4.65971       -2.24843
   C        1.65707        5.05619        0.46680
   H        1.14965        5.49697        1.34832
   H        2.29662        5.83875        0.00438
   H        2.33007        4.25771        0.84055
   H        2.39691       -1.38756        1.19559
   H        1.97188        0.12750        2.02423
   H        2.62857        0.15089        0.33872
end

basis
  * library 6-31G*
end

dft
  xc b3lyp
```

```
  mult 1
end

task dft optimize

task dft freq
```

Table B.1: Cartesian coordinates used for the calculation of Raman vibrational modes of vitamin A.

atom	x	y	z
C	-0.14521	5.61033	-1.18986
C	0.72594	4.47366	-0.60768
C	-0.14856	3.42792	0.12729
C	-1.42063	3.68995	0.52154
C	-2.12109	5.00081	0.21319
C	-1.17972	6.13379	-0.19721
H	-2.71791	5.30200	1.08539
H	-2.85682	4.82197	-0.58923
H	-0.67920	6.53829	0.69186
H	-1.75078	6.96169	-0.63553
H	-0.67032	5.23238	-2.07900
H	0.51058	6.42038	-1.53628
C	0.53431	2.14795	0.39854
C	0.03866	0.90789	0.17937

continued on next page

Continuation of Table B.1

atom	x	y	z
C	0.72589	-0.35329	0.42215
C	0.07747	-1.51306	0.10801
C	2.11766	-0.30894	1.00512
C	0.54652	-2.86759	0.25301
C	-0.19559	-3.94824	-0.10030
C	0.20015	-5.34536	0.01083
C	1.56634	-5.66913	0.57297
H	2.35960	-5.21303	-0.03271
H	1.75513	-6.74492	0.61053
H	1.67631	-5.27631	1.59164
C	-0.66132	-6.30530	-0.39059
C	-0.43647	-7.79169	-0.35628
O	-1.60867	-8.41128	-0.87645
H	-0.23706	-8.13138	0.67568
H	0.45110	-8.06455	-0.95443
H	-1.47022	-9.36975	-0.85714
H	1.56336	2.23030	0.74719
H	-0.96282	0.81879	-0.23919
H	-0.92640	-1.41613	-0.30801
H	1.54054	-3.02509	0.66344
H	-1.19056	-3.77415	-0.51163
H	-1.63304	-6.01762	-0.78833
C	-2.28426	2.73059	1.30828

continued on next page

Continuation of Table B.1

atom	x	y	z
H	-1.71726	1.90527	1.74159
H	-3.07759	2.29751	0.68108
H	-2.79517	3.26467	2.12070
C	1.47713	3.81716	-1.78834
H	0.77786	3.32996	-2.47738
H	2.19488	3.06091	-1.45489
H	2.03188	4.57920	-2.35024
C	1.76962	5.06213	0.37343
H	1.29120	5.58385	1.20852
H	2.42233	5.77500	-0.14644
H	2.41127	4.28214	0.79814
H	2.53768	-1.30279	1.16922
H	2.12163	0.21855	1.96739
H	2.80268	0.23567	0.34218

End of Table B.1

Bibliography

[1] C. Garhart, V. Lakshminarayanan, and W. W. Y. Li. *Anatomy of the Eye*. Springer, Berlin, Heidelberg, 2012.

[2] P. Brodal. *The Central Nervous System: Structure and Function*. Oxford University Press, New York, 2010.

[3] M. Gupta, A. Herzlich, T. Sauer, and C.-C. Chan. Retinal Anatomy and Pathology. *Developments in ophthalmology*, 2015, doi: 10.1159/000431128.

[4] H. Purnyn. The Mammalian Retina: Structure and Blood Supply. *Neurophysiology; New York*, 2013, doi: 10.1007/s11062-013-9365-6.

[5] M. W. Ansari and A. Nadeem. *The Eyeball: Some Basic Concepts*. Springer International Publishing, 2016.

[6] J. C. Saari. Vitamin A Metabolism in Rod and Cone Visual Cycles. *Annual Review of Nutrition*, 2012, doi: 10.1146/annurev-nutr-071811-150748.

[7] P. Chen, T. D. Lee, and H. K. W. Fong. Interaction of 11-cis-Retinol Dehydrogenase with the Chromophore of Retinal G Protein-coupled Receptor Opsin. *Journal of Biological Chemistry*, 2001, year.

[8] M. Cascella, S. Bärfuss, and A. Stocker. Cis-retinoids and the chemistry of vision. *Archives of Biochemistry and Biophysics*, 2013, doi: 10.1016/j.abb.2013.06.003.

[9] T. Maeda, M. Golczak, and A. Maeda. Retinal Photodamage Mediated by All-trans-retinal. *Photochemistry and Photobiology*, 2012, doi: 10.1111/j.1751-1097.2012.01143.x.

[10] P. Victor R. *Vitamin A and Carotenoids : Chemistry, Analysis, Function and Effects*. Number no. 1 in Food and Nutritional Components in Focus. Royal Society of Chemistry, 2012.

[11] N. Failloux, I. Bonnet, M.-H. Baron, and E. Perrier. Quantitative Analysis of Vitamin A Degradation by Raman Spectroscopy. *Applied Spectroscopy*, 2003, year.

[12] A.-A. Arteni, M. Fradot, D. Galzerano, M. M. Mendes-Pinto, J.-A. Sahel, S. Picaud, B. Robert, and A. A. Pascal. Structure and Conformation of the Carotenoids in Human Retinal Macular Pigment. *PloS one*, 2015, doi: 10.1371/journal.pone.0135779.

[13] L. Ma and X.-M. Lin. Effects of lutein and zeaxanthin on aspects of eye health. *Journal of the Science of Food and Agriculture*, 2009, doi: 10.1002/jsfa.3785.

[14] author = Agnieszka Sujak and Janina Gabrielska and Wojciech Grudziński and Robert Borc and Piotr Mazurek and Wiesław I. Gruszecki. Lutein and Zeaxanthin as Protectors of Lipid Membranes against Oxidative Damage: The Structural Aspects. *Archives of Biochemistry and Biophysics*, 1999, year.

[15] R. A. Bone, J. T. Landrum, L. M. Friedes, C. M. Gomez, M. D. Kilburn, E. Menendez, I. Vidal, and W. Wang. Distribution of Lutein and Zeaxanthin Stereoisomers in the Human Retina. *Experimental Eye Research*, 1997, doi: 10.1006/exer.1996.0210.

[16] Q. Li, A. Verma, A. Dinculescu, A. S. Lewin, and W. W. Hauswirth. NADPH Oxidase in Choroidal Neovascularization. In *Studies on Retinal and Choroidal Disorders*. Humana Press, Totowa, NJ, 2012.

[17] P. S. Bernstein, M. D. Yoshida, N. B. Katz, R. W. McClane, and W. Gellermann. Raman detection of macular carotenoid pigments in intact human retina. *Investigative Ophthalmology & Visual Science*, 1998, year.

[18] B. Li and P. S. Bernstein. *Macular Pigment Carotenoids and Their Roles in Human Eye Health and Diseases*. Humana Press, Totowa, NJ, 2012.

[19] J. M. Nolan. *The Role of the Macular Carotenoids as a Blue Light Filter and an Antioxidant*. Humana Press, Totowa, NJ, 2012.

[20] M. Yu, R. E. Anderson, and N. A. Mandal. *Natural Compounds in Retinal Diseases*. Humana Press, Totowa, NJ, 2012.

[21] A. Nunes and S. Magalhães. *Raman Spectroscopy*, chapter Raman Spectroscopy Applied to Health Sciences. IntechOpen, 2018.

[22] P. Vandenabeele. Raman Spectroscopy Applied to Health Sciences. *Analytical and Bioanalytical Chemistry*, 2010, doi: http://dx.doi.org/10.1007/s00216-010-3872-8.

[23] P. Vandenabeele and D. J. Ando. *Practical Raman Spectroscopy: An Introduction*. John Wiley & Sons, Incorporated, Hoboken, United Kingdom, 2013.

[24] P. Larkin. *IR and Raman Spectroscopy: Principles and Spectral Interpretation*. Elsevier, Saint Louis, United States of America, 2011.

[25] N. B. Colthup, L. H. Daly, and S. E. Wiberley. *Introduction to Infrared and Raman Spectroscopy*. Academic Press, New York, United States of America, 1975.

[26] M. Z. Pacia, K. Czamara, M. Zebala, E. Kus, S. Chlopicki, and A. Kaczor. Rapid diagnostics of liver steatosis by Raman spectroscopy via fiber optic probe: a pilot study. *Analyst*, 2018, doi: 10.1039/C8AN00289D.

[27] S. Mazurek, K. Pichlak, and R. Szostak. Quantitative Determination of Vitamins A and E in Ointments Using Raman Spectroscopy. *Processes*, 2021, year.

[28] R. G. Reifenberger. *Fundamentals Of Atomic Force Microscopy - Part I: Foundations*. World Scientific, Singapore, 2016.

[29] P. Eaton and P. West. *Atomic Force Microscopy*. Oxford University Press, New York, 2010.

[30] B. Voigtlander. Amplitude Modulation (AM) Mode in Dynamic Atomic Force Microscopy. In *Scanning Probe Microscopy: Atomic Force Microscopy and Scanning Tunneling Microscopy*. Springer, Berlin Heidelberg, 2015.

[31] N. Gavara. A beginner's guide to atomic force microscopy probing for cell mechanics. *Microscopy Research and Technique*, 2017, doi: 10.1002/jemt.22776.

[32] *A Tutorial on the Mechanisms, Dynamics, and Control of Atomic Force Microscopes*, volume 1, New York City, USA, 2007.

[33] C. M. Franz and P.-H. Puech. Atomic Force Microscopy: A Versatile Tool for Studying Cell Morphology, Adhesion and Mechanics. *Cellular and Molecular Bioengineering*, 2008, doi: 10.1007/s12195-008-0037-3.

[34] H. Fortier, F. Variola, C. Wang, and S. Zou. AFM force indentation analysis on leukemia cells. *Analytical Methods*, 2016, doi: 10.1039/C6AY00131A.

[35] B. Pettinger, K. F. Domke, D. Zhang, G. Picardi, and R. Schuster. Tip-enhanced Raman scattering: Influence of the tip-surface geometry on optical resonance and enhancement. *Surface Science*, 2009, doi: 10.1016/j.susc.2008.08.033.

[36] E. Bailo and V. Deckert. Tip-Enhanced Raman Scattering. *Chemical Society Reviews*, 2008, doi: https://doi.org/10.1039/B705967C.

[37] R. Eric Le and E. Pablo. *Principles of Surface-Enhanced Raman Spectroscopy : And Related Plasmonic Effects.*, volume 1st ed. Elsevier Science, 2009.

[38] L. Langeluddecke, P. Singh, and V. Deckert. Exploring the Nanoscale: Fifteen Years of Tip-Enhanced Raman Spectroscopy. *Applied Spectroscopy*, 2015, year.

[39] G. Sharma, T. Deckert-Gaudig, and V. Deckert. Tip-enhanced Raman scattering–Targeting structure-specific surface characterization for biomedical samples. *Advanced Drug Delivery Reviews*, 2015, doi: 10.1016/j.addr.2015.06.007.

[40] C. C. Neacsu, S. Berweger, and M. B. Raschke. Tip-Enhanced Raman Imaging and Nanospectroscopy: Sensitivity, Symmetry, and Selection Rules. *Nanobiotechnology; Dordrecht*, 2007, doi: 10.1007/s12030-008-9015-z.

[41] T. Yano, T. Ichimura, A. Taguchi, N. Hayazawa, P. Verma, Y. Inouye, and S. Kawata. Confinement of enhanced field investigated by tip-sample gap regulation in tapping-mode tip-enhanced Raman microscopy. *Applied Physics Letters*, 2007, doi: 10.1063/1.2785115.

[42] T. Ichimura, S. Fujii, P. Verma, T. Yano, Y. Inouye, and S. Kawata. Subnanometric Near-Field Raman Investigation in the Vicinity of a Metallic Nanostructure. *Physical Review Letters*, 2009, doi: 10.1103/PhysRevLett.102.186101.

[43] Z. Yang, J. Aizpurua, and H. Xu. Electromagnetic field enhancement in TERS configurations. *Journal of Raman Spectroscopy*, 2009, doi: 10.1002/jrs.2429.

[44] T. Deckert-Gaudig and V. Deckert. Tip-enhanced Raman scattering (TERS) and high-resolution bio nano-analysis–a comparison. *Physical Chemistry Chemical Physics*, 2010, doi: 10.1039/C003316B.

[45] N. Kumar, S. Mignuzzi, W. Su, and D. Roy. Tip-enhanced Raman spectroscopy: principles and applications. *EPJ Techniques and Instrumentation*, 2015, doi: 10.1140/epjti/s40485-015-0019-5.

[46] T. Deckert-Gaudig, A. Taguchi, S. Kawata, and V. Deckert. Tip-enhanced Raman spectroscopy – from early developments to recent advances. *Chemical Society Reviews*, 2017, doi: 10.1039/C7CS00209B.

[47] K. C. Brown. Mapping Vitamin A in the Retina. Honours thesis, Memorial University Newfoundland and Labrador, 2019.

[48] M. D. Hanwell, D. E. Curtis, D. C. Lonie, T. Vandermeersch, E. Zurek, and G. R. Hutchison. Avogadro: An advanced semantic chemical editor, visualization, and analysis platform. *Journal of Cheminformatics*, 2012, year.

[49] E. Aprà, E. J. Bylaska, W. A. de Jong, N. Govind, K. Kowalski, T. P. Straatsma, M. Valiev, H. J. J. van Dam, Y. Alexeev, J. Anchell, V. Anisimov, F. W. Aquino, R. Atta-Fynn, J. Autschbach, N. P. Bauman, J. C. Becca, D. E. Bernholdt, K. Bhaskaran-Nair, S. Bogatko, P. Borowski, J. Boschen, J. Brabec, A. Bruner,

E. Cauët, Y. Chen, G. N. Chuev, C. J. Cramer, J. Daily, M. J. O. Deegan, T. H. D. Jr., M. Dupuis, K. G. Dyall, G. I. Fann, S. A. Fischer, A. Fonari, H. Früchtl, L. Gagliardi, J. Garza, N. Gawande, S. Ghosh, K. Glaesemann, A. W. Götz, J. Hammond, V. Helms, E. D. Hermes, K. Hirao, S. Hirata, M. Jacquelin, L. Jensen, B. G. Johnson, H. Jónsson, R. A. Kendall, M. Klemm, R. Kobayashi, V. Konkov, S. Krishnamoorthy, M. Krishnan, Z. Lin, R. D. Lins, R. J. Littlefield, A. J. Logsdail, K. Lopata, W. Ma, A. V. Marenich, J. M. del Campo, D. Mejia-Rodriguez, J. E. Moore, J. M. Mullin, T. Nakajima, D. R. Nascimento, J. A. Nichols, P. J. Nichols, J. Nieplocha, A. O. de-la Roza, B. Palmer, A. Panyala, T. Pirojsirikul, B. Peng, R. Peverati, J. Pittner, L. Pollack, R. M. Richard, P. Sadayappan, G. C. Schatz, W. A. Shelton, D. W. Silverstein, D. M. A. Smith, T. A. Soares, D. Song, M. Swart, H. L. Taylor, G. S. Thomas, V. Tipparajua, D. G. Truhlar, K. Tsemekhman, T. Van Voorhis, Á. Vázquez-Mayagoitia, P. Verma, O. Villa, A. Vishnu, K. D. Vogiatzis, D. Wang, J. H. Weare, M. J. Williamson, T. L. Windus, K. Woliński, A. T. Wong, Q. Wu, C. Yang, Q. Yu, M. Zacharias, Z. Zhang, Y. Zhao, and R. J. Harrison. NWChem: Past, present, and future. *The Journal of Chemical Physics*, 2020, doi: 10.1063/5.0004997.

[50] J. P. Cerón-Carrasco, A. Bastida, J. Zúñiga, A. Requena, and B. Miguel. Density Functional Theory Study of the Stability and Vibrational Spectra of the β-Carotene Isomers. *J. Phys. Chem. A*, 2009, doi: https://doi-org.qe2a-proxy.mun.ca/10.1021/jp9037446.

[51] W. Liu, Z. Wang, Z. Zheng, L. Jiang, Y. Yang, L. Zhao, and W. Su. Density Functional Theoretical Analysis of the Molecular Structural Effects on Raman Spectra of β-Carotene and Lycopene. *Chin. J. Chem*, 2012, doi: http://dx.doi.org/10.1002/cjoc.201200661.

[52] T. S., C. A., T. O. Mendes, L. dos Santos, M. G. P. Silva, L. Pereira, P. Fávero, P. Singh, and A. A. Martin. Combined in vivo confocal Raman spectroscopy and density functional theory to detect carboxymethyl(lysine) in the human stratum corneum. *J Vibrational Spectroscopy*, 2019, doi: https://doi.org/10.1016/j.vibspec.2018.10.005.

[53] S. L. Christian, N. K. Pallegar, R. J. Brown, and A. M. Viloria-Petit. Collagen overlays can inhibit leptin and adiponectin secretion but not lipid accumulation in adipocytes. *PeerJ*, 2018, doi: 10.7717/peerj.4641.

[54] M. Mahmoud, L. Cancel, and J. M. Tarbell. Matrix Stiffness Affects Glycocalyx Expression in Cultured Endothelial Cells. *Front. Cell Dev. Biol.*, 2021, doi: doi: 10.3389/fcell.2021.731666.

[55] S. Ricard-Blum. The Collagen Family. *Cold Spring Harbor Perspectives in Biology*, 2011, doi: 10.1101/cshperspect.a004978.

[56] M. D. Shoulders and R. T. Raines. Collagen Structure and Stability. *Annual Review of Biochemistry*, 2009, doi: 0.1146/annurev.biochem.77.032207.120833.

[57] M. E. Henriques and M. Pinto. *Type I collagen biological functions, synthesis and medicinal applications.* Nova Science Publishers, Inc, New York, 2012.

[58] D. R. Stamov, A. Müller, Y. Wegrowski, S. Brezillon, and C. M. Franz. Quantitative analysis of type I collagen fibril regulation by lumican and decorin using AFM. *Journal of Structural Biology*, 2013, doi: 10.1016/j.jsb.2013.05.022.

[59] K. Gelse, E. Pöschl, and T. Aignera. Collagens–structure, function, and biosynthesis. *Advanced Drug Delivery Reviews*, 2003, doi: 10.1016/j.addr.2003.08.002.

[60] Z. Dong. Collagen matrices: biomaterials for selective cell response. Master's thesis, Memorial University Newfoundland and Labrador, 2017.

[61] F. C., S. KM., and W. VM. The extracellular matrix at a glance. *J Cell Sci.*, 2010, doi: 10.1242/jcs.023820.

[62] H.-J. Butt. Measuring electrostatic, van der Waals, and hydration forces in electrolyte solutions with an atomic force microscope. *Biophysical Journal*, 1991, doi: https://doi.org/10.1016/S0006-3495(91)82180-4.

[63] W. A. Ducker, T. J. Senden, and R. M. Pashley. Direct measurement of colloidal forces using an atomic force microscope. *Nature*, 1991, doi: https://doi.org/10.1038/353239a0.

[64] H.-J. Butt, B. Cappella, and M. Kappl. Force measurements with the atomic force microscope: Technique, interpretation and applications. *Surface Science Reports*, 2005, doi: 10.1016/j.surfrep.2005.08.003.

[65] A. Mark, N. Helfricht, A. Rauh, M. Karg, and G. Papastavrou. The Next Generation of Colloidal Probes: A Universal Approach for Soft and Ultra-Small Particles. *Small (Weinheim an der Bergstrasse, Germany)*, 2019, doi: 10.1002/smll.201902976.

[66] J. Ralston, I. Larson, M. W. Rutland, A. A. Feiler, and M. Kleijn. Atomic force microscopy and direct surface force measurements (IUPAC Technical Report). *Pure and Applied Chemistry*, 2005, doi: 10.1351/pac200577122149.

[67] WaveMetrics Inc. *Igor Pro (5).* http://www.wavemetrics.com, USA.

[68] K. Johnson, K. Kendall, and A. Roberts. Surface energy and the contact of elastic solids. *Proc. R. Soc. Lond. A.*, 1971, year.

[69] I. Jorba, J. J. Uriarte, N. Campillo, R. Farré, and D. Navajas. Probing Micromechanical Properties of the Extracellular Matrix of Soft Tissues by Atomic Force Microscopy. *Journal of Cellular Physiology*, 2017, year.

[70] D. Herman and J. Y. Walz. Forces and force-scaling in systems of adsorbing nanoparticles as measured using colloidal probe atomic force microscopy. *Colloids and Surfaces A*, 2015, doi: https://doi.org/10.1016/j.colsurfa.2015.04.053.

[71] S. R. Pereira. How to do Raman simulations using NWChem 6.6 and Ace net servers. 2020.